Mirjam Skof, BSc

Influence of Earth Alkaline Dopants on the Properties of Lanthanum Modified Lead Zirconate Titanate

MASTER THESIS

For obtaining the academic degree
Diplom-Ingenieurin

Master Program of
Advanced Materials Science

Graz University of Technology

Supervisor:
Ao.Univ.-Prof. Dipl.-Ing. Dr.techn. Klaus Reichmann
Institute for Chemistry and Technology of Materials

Graz, August 2013

Deutsche Fassung:
Beschluss der Curricula-Kommission für Bachelor-, Master- und Diplomstudien vom 10.11.2008
Genehmigung des Senates am 1.12.2008

EIDESSTATTLICHE ERKLÄRUNG

Ich erkläre an Eides statt, dass ich die vorliegende Arbeit selbstständig verfasst, andere als die angegebenen Quellen/Hilfsmittel nicht benutzt, und die den benutzten Quellen wörtlich und inhaltlich entnommenen Stellen als solche kenntlich gemacht habe.

Graz, am …… ……..
(Unterschrift)

Englische Fassung:

STATUTORY DECLARATION

I declare that I have authored this thesis independently, that I have not used other than the declared sources / resources, and that I have explicitly marked all material which has been quoted either literally or by content from the used sources.

…… ……..
date (signature)

Danksagung

Für das interessante Thema und die ausgezeichnete Betreuung während der Arbeit möchte ich mich bei meinem Betreuer Herrn Ao. Univ.-Prof. Dipl.-Ing Dr. Klaus Reichmann bedanken.

Mein Dank für die Unterstützung gilt außerdem der Christian Doppler Gesellschaft und der EPCOS OHG, einem Mitglied der TDK-EPC Gruppe.

Ich danke außerdem der Arbeitsgruppe für die gute Zusammenarbeit und Unterstützung.

Weites möchte ich mich bei Frau Sanja Simic, Frau Dipl.-Ing. Dr. Brigitte Bitschnau, Herrn Ao. Univ.-Prof. Dipl.-Ing. Dr. Franz Mautner und Ao.Univ.-Prof. Dipl.-Ing. Dr. Otto Fruhwirth für die Durchführung der Messungen am Elektronenmikroskop, Röntgendiffraktometer und Dilatometer bedanken.

Mein Dank gebührt auch meiner Familie, die mir dieses Studium überhaupt erst ermöglicht hat.

Danke auch an meinen Freund Daniel und meine Freunde Theresa, Simone, Stefanie, Christian und Ian für gemeinsames Lernen, interessante Diskussionen und generell dafür bedanken, dass sie für mich da sind, wenn ich sie brauche.

Abstract

In this study the influence of earth alkaline dopants, such as Ba, Ca and Sr on the properties of lanthanum modified lead zirconate – lead titanate (PLZT) ceramics should be investigated. Therefore two basic compositions of PLZT with differing Zr-/Ti-content were mixed with varying concentrations of Ba, Ca and Sr according to the following formula: $(Pb_{0,91-x-y-z}Ba_xCa_ySr_zLa_{0,06})(Zr_{1-m}Ti_m)O_3$ (x, y, z = 0 & 0,02, m = 0,10 & 0,15).

The ceramic powders were processed via the mixed oxide route, calcined at 925°C and sintered at 1250°C. An excess of 2 % lead was added prior calcination. After the preparation the samples were examined with XRD to control the formation of the perovskite structure.

In order to analyze the microstructure the samples needed to be polished with silica gel and sputtered with carbon, then, via channeling contrast mode in SEM, images could have been taken. Antecedent poling enabled the investigation of the domain structure. In addition the average grain size for every composition was evaluated with the line section method. Backscattered and secondary electron imaging was used to identify secondary phases.

The dielectric properties were measured by determining the permittivity, the loss factor and the piezoelectric constant d_{33}. Furthermore low and high signal measurements were carried out.

The results were compared according to the chemical composition of the samples. All samples could have been sintered at the same temperature regardless of composition; however the importance of the set-up for sintering was shown. While there is a difference in relative densities of 2,6 % between the non-doped samples, the values start to assimilate for the fully doped mixtures. A similar effect was found during the grain size studies in the SEM images.

Low as well as high signal measurements showed a significant influence of the Zr/Ti-ratio as well as of dopant concentration on the dielectric properties, such as relative

permittivity, switching field and energy loss during hysteresis. In contrast to the PLZT (6/85/15)-samples, the PLZT (6/90/10)-compositions did not yield significant results in the high signal measurements due to the fact, that the breakdown voltage of all samples of this compositions is below the switching field.

Kurzfassung

Im Rahmen der Arbeit wurden die Einflüsse von Erdalkali-Dotierstoffen (Ca, Sr, Ba) auf die Eigenschaften von zwei Mischungen aus Blei Zirkonat - Blei Titanat mit unterschiedlichem Zirkon-Titan-Verhältnis untersucht. Die verwendeten Zusammensetzungen lauteten, wie anhand folgender Formel ersichtlich, $(Pb_{0,91-x-y-z}Ba_xCa_ySr_zLa_{0,06})(Zr_{1-m}Ti_m)O_3$ (x, y, z = 0 & 0,02, m = 0,10 & 0,15).

Die Probenherstellung erfolgte über die Mischoxidmethode, die Kalzinierungs- und Sinterungstemperaturen betrugen 925°C bzw 1250°C. Zum Ausgleich des Bleiverlusts wurde dem unkalzinierten Probenpulver ein Überschuss von 2 % Blei zugegeben. Zur Bestimmung der Kristallstruktur wurden die umgesetzten Probenpulver mittels XRD untersucht.

Die Analyse der Mikrostruktur der gesinterten Keramik erfolgte mittels Channeling-Kontrast Modus im Rasterkraftmikroskop. Hierfür wurden die Probenkörper mit Hilfe von Silicagel poliert und mit Kohlenstoff besputtert. Eine vor der Untersuchung durchgeführte Polung erlaubte die Aufnahme der Domänenstruktur im Probekörper. Mittels der Line-Section-Methode konnte die durchschnittliche Korngröße bestimmt werden. Über die Aufnahme von Rückstreu- und Sekundärelektronenbildern wurden Sekundärphasen im Probenkörper identifiziert.

Die Messung der dielektrischen Eigenschaften erfolgte über die Bestimmung der Permittivität, des Verlustfaktors sowie der Piezoelektrischen Konstante $d_{33.}$ Außerdem wurden Klein- sowie Großsignalmessungen durchgeführt.

Die erhaltenen Resultate wurden je nach der chemischen Zusammensetzung der jeweiligen Proben ausgewertet. Während die Proben unabhängig von ihrer Zusammensetzung sehr ähnliche Sintertemperaturen aufwiesen, konnte gezeigt werden, dass speziell der Aufbau während des Sintervorganges einen sehr starken Einfluss auf die resultierenden Dichten der Proben hat. Die Messungen der relativen Dichte zeigten einen Unterschied der nicht dotierten Proben von 2,6 %, mit steigender Dotierstoffkonzentration glichen sich die Werte jedoch an. Ein ähnlicher Effekt stellte sich auch bei der Korngröße der gesinterten Keramiken ein.

Klein- sowie Großsignalmessungen zeigten sowohl einen starken Einfluss des Zr/Ti-Verhältnisses als auch der Dotierstoffe auf die dielektrischen Eigenschaften, wie der relativen Permittivität, dem Schaltfeld und dem Energieverlust während der Hysterese. Für die PLZT (6/90/10)-Mischungen konnten aufgrund der, verglichen mit den benötigten hohen Feldern, niedrigen Durchschlagsfestigkeit, keine aussagekräftigen Werte bei den Großsignalmessungen gewonnen werden. Die PLZT (6/85/15)-Mischungen hingegen erlaubten es, eine Aussage bezüglich des Einflusses der Dotierstoffe auf das Schaltfeld zu treffen.

Table of Contents

Danksagung ..... *i*

Abstract ..... *i*

Kurzfassung ..... *iii*

Table of Contents ..... *v*

1 Motivation and Objectives *1*

2 Basics and Theoretic Background *2*

2.1 Polarization Mechanisms **3**

2.1.1 Domain Structures 4

2.2 Dielectric Properties [3] **6**

2.2.1 Ferroelectricity 8

2.2.1.1 Phase Stability 9

2.2.2 Antiferroelectricity 10

2.2.2.1 Antiferroelectric Materials [9] 11

2.3 The System PZT **11**

2.3.1 Influence of Substituents 12

2.3.1.1 Lanthanum as Dopant for PZT 13

2.4 Processing PLZT **14**

2.4.1 Powder Preparation 14

2.4.1.1 Comminution 15

2.4.2 Synthesis 15

2.4.2.1 Solid State Reactions 15

2.4.3 Sintering and Microstructural Development 16

2.4.3.1 Forming 17

2.4.3.2 The Sintering Process 17

2.4.4 Defect Chemistry 23

2.4.4.1 Defect Types 23

3 Materials and Methods *25*

3.1 Sample Processing **25**

3.2 Preparation of the Sample Powders **26**

3.3 Formation of the Green Bodies **27**

3.4 Sintering Experiments 28
3.4.1 Sinter Temperature and Dilatometric Analysis 29
3.5 Sample Characterization 30
3.5.1 Calcination Weight Loss 30
3.5.2 Density Studies 30
3.5.3 Shrinkage Studies 30
3.5.4 X-Ray Diffraction and Crystal Structure Analysis 31
3.5.5 Scanning Electron Microscopy 31
3.5.6 Dielectric and Piezoelectric Properties 31
4 Results 33
4.1 Pretesting 33
4.1.1 Effective Mass vs. Tolerance Factor 33
4.1.2 Dilatometry 34
4.2 Measurements for Process Control 36
4.2.1 Calcination Weight Loss 36
4.2.2 Influence of Sinter Beddings on the Density 37
4.2.3 X-Ray Diffraction Analysis 38
4.2.4 Densities of the Sintered Samples 41
4.2.5 Shrinkage Studies 42
4.2.6 Electron Microscopy Analysis 43
4.3 Electric Characterization 45
4.3.1 Piezoelectric Constant d_{33} 45
4.3.2 I90: PLZT (6/90/10) 47
4.3.2.1 Low Signal Measurements 47
4.3.2.2 High Signal Measurements 49
4.3.3 M85: PLZT (6/85/15) 50
4.3.3.1 Low Signal Measurements 50
4.3.3.2 High Signal Measurements 52
5 Summary 56
6 Appendix 59
6.1 X-Ray Diffraction Analysis 59
6.1.1 Densities of the Sintered Samples 60
6.2 Electron Microscopy Analysis 61
6.2.1 SEM-Images 61

6.2.2 Images for EDX Analysis 63

6.3 M85: PLZT (6/85/15)..... 64

6.3.1 Electric Characterization 64

7 References 65

8 List of Figures 67

9 List of Tables 69

1 Motivation and Objectives

In this work the influence of alkaline earth dopants, such as barium, calcium and strontium on the antiferroelectric properties of lanthanum modified lead zirconate-titanate was examined. In addition the effect of a different zirconium/titanium-ratio also was analyzed.

The change in properties, such as switching field due to the doping with those isovalent ions has been positioned within taxonomy according to the differences in the ionic radii and masses.

A number of investigations have already been performed on the change in the antiferroelectric properties of each barium-, calcium- or strontium-doped PLZT but there are no references of studies where a combination of these ions was analyzed.

The aim was to perform a systematic research not only on how each of those dopants will influence the properties of the basic material when used as the only dopant, as it already can be found in the literature, but also how a combination of the alkaline earth ions will change the properties. Furthermore a possible synergy of the effects of the single dopants was studied.

2 Basics and Theoretic Background

Unless otherwise noted the following section is an excerpt from the book of A. J. Moulson and J. M. Herbert, “Electroceramics”, see Ref. [1]. Further sources are indicated separately.

The positions of ions arranged in a solid are defined by their charge and size. The first determines the order of the ions while the second one determines the way they are packed and hence the crystal structure.

In oxides, the structure is built of arrangements of O^{2-} ions, such as e.g. in perovskites (ABO_3). The structure can be seen as a matrix of corner-sharing BO_6 octahedra with large cations (A) filling the interstitial sites. The A site is often occupied by an alkaline or earth-alkaline metal as well as a lanthanide ions while B normally represents a transition-metal ion [2].

To allow a prediction of the likelihood of an ion to occupy either of the mentioned sites the concept of ionic radii is quite useful. In order to determine the size of an ion inside a solid one either uses X-ray structure analysis and calculates the radii from electron density maps or one defines the ions as rigid spheres where the distance between the centers of neighboring ions is taken and divided in half. Since this fairly simple approximation does neglect the quantum mechanical point of view, not only the atomic number but also the charge of the ion as well as its nearest neighbors needs to be taken into account additionally.

A further forecast about the stability of a crystal structure, such as the perovskite structure, is given by Goldschmidt’s tolerance factor (t-factor).

$$t = \frac{(R_A + R_O)}{\sqrt{2}\,(R_B + R_O)} \qquad (1)$$

with R_A, R_B and R_O signifying the radii of the ions on the indicated site. In case of t = 1, the structure is an ideal perovskite while t > 1 and t < 1 represent ferroelectric (polar) and antiferroelectric (non-polar) structures respectively. [3]

2.1 Polarization Mechanisms

The over-all polarizability of a material can be separated in four parts:

a) an electronic one, resulting from de-alignment of electrons and the atomic nucleus relative to one another
b) an ionic one, resulting from the de-alignment of positive and negative ions within the sublattice
c) a part resulting from the rearrangement of permanent dipole
d) and the formation of space charges at interfaces.

The polarizability is strongly depended on the frequency, since with higher frequencies the movement of the ions and molecules will be too slow to be taken into account. [4]

Taking a deeper look on crystal structures one finds 11 centrosymmetric, and hence non-piezoelectric, as well as 21 non-centrosymmetric crystal classes, of which 20 show the piezoelectric effect. Among those 20 structures 10 are of polar nature. Due to this fact they can be seen as both, piezo- and pyroelectric.

In some pyroelectric materials the direction of the polarization can be changed by exposing the material to an electric field. In that case the material is called ferroelectric. This procedure is known as poling, it aligns the materials polar axis to the direction of the electric field. Limitations are due to the crystal structure as well as local environmental influences, such as grains or phase boundaries, since the process of poling requires small rearrangements of the charge carriers.

A dipole can be described as two equal point charges separated by a distance, aligning these dipoles in such way, that every negative point charge faces a positive point charge within a long line one creates a stylized model of a polarized material.

The dipole moment ***p***, a vector pointing from the negative to the positive charge, can be described as

$$\vec{p} = Q\delta x \qquad (2)$$

Thus leading to the polarization, that is defined as the dipole moment per unit volume, its value can change within the material. Equation $\delta \mathrm{p} = \sigma_\mathrm{P} \mathrm{A} \delta \mathrm{x} = \sigma_\mathrm{P} \delta \mathrm{V}$ (3(3) describes the vectors used, thus leading to Equation (4).

$$\delta \mathrm{p} = \sigma_\mathrm{P} \mathrm{A} \delta \mathrm{x} = \sigma_\mathrm{P} \delta \mathrm{V} \ (3)$$

$$\frac{\delta \mathrm{p}}{\delta \mathrm{V}} = \mathrm{P} = \sigma_\mathrm{P} \quad (4)$$

where σ_P is the polarization multiplied by the unit vector normal to the surface, directing away from the material and enclosing the polarized material.

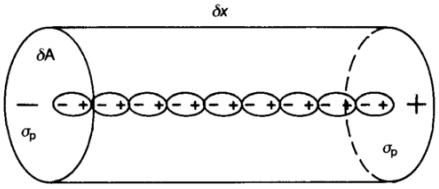

Figure 1: schematic of a polarized material [1]

2.1.1 Domain Structures

Having a body affected by an electric field $\boldsymbol{E_a}$, a depolarization field $\boldsymbol{E_{dp}}$ on the surface is occurring, resulting in an internal macroscopic field $\boldsymbol{E_m}$ that opposes $\boldsymbol{E_{dp}}$. A similar mechanism is available for materials affected by spontaneous polarization.

Ferroelectric domains can be seen as regions where the spontaneous polarization, in this case a vector, has the same direction and absolute value. By forming domains and separating the crystal into oppositely polarized regions, the energy of the depolarization field resulting from the spontaneous polarization is minimized. For every polar axis either direction, be it positive or negative, has the same likelihood to arise. Therefore the directions for such domains can be randomly picked, not only in an antiferroelectric way but also determined by the crystal structure. Surrounding the ferroelectric solid, an electric field arises. The amount of domains is inversely proportional to the size of the outer field and hence the energy. In the following

picture this theory is explained, furthermore an ideal arrangement of 90° domains is shown. [5]

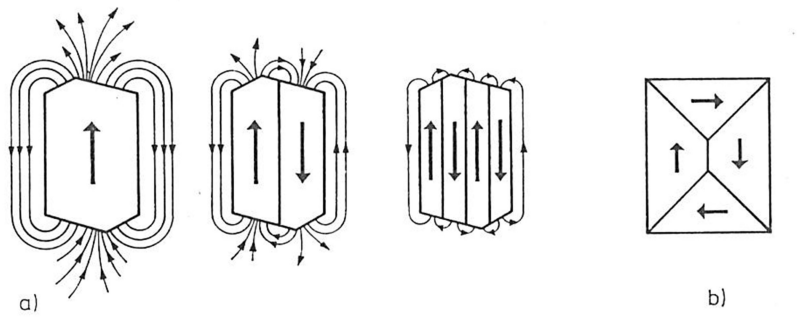

Figure 2: schematic of a domain structure [5], a) minimizing the size of the outer field and hence the energy by forming multi-domains, b) ideal arrangement of 90° domains

In between the 180° domains, where the spontaneous polarization is reversed, the following contributions to the wall energy need to be taken into account:

1) Correlation energy arising from the spatial change in polarization
2) Electrostriction energy evolving from interactions between polarization and crystal deformation
3) Change of free enthalpy when varying the spontaneous polarization.

All of those contributions lead to an increased energy density per volume in relation to the domains itself. [5]

When applying an external electric field pointing into either of those polar directions, this multi-domain arrangement can be transformed into a single-domain state. For reversing this effect, a field oriented into the opposite direction of the applied field, a high a.c. field or mechanical stress can be applied. For a full depoling, the ceramic needs to be heated first to temperatures above the Curie-Temperature T_c and then cooled down without been exposed to an electric field.

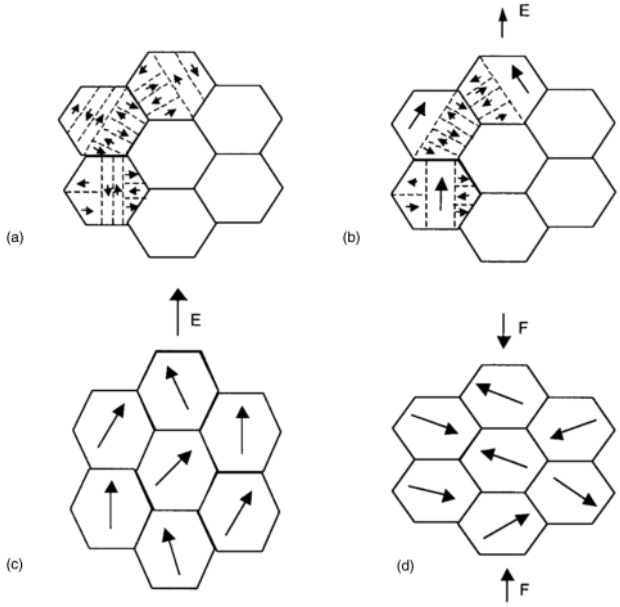

**Figure 3: illustration of a domain structure changing according to outer influences [1];
a) initial state, non-polar grains; b) applied electric field, net-polarity is formed;
c) elongation and switching of domains under increasing applied field;
d) disorientation of domains due to applied stress**

2.2 Dielectric Properties [3]

As already discussed above, a dielectric material in an electric field is forced to slightly rearrange its charge carriers in order to obtain a dipole moment and therefore to be polarized. Depending on the resultant polarization, dielectrics can be classified according to their behavior when a driving electric field is applied, either as linear or as non-linear. Hysteresis loops, as shown in the figure below, are used to gain information about these characteristics.

Applying a static electric field to a non-conducting dielectric material, leads to the following relationship:

$$D = \varepsilon_0 E + P = \varepsilon E \quad (5)$$

With the permittivity of the dielectric ε, the permittivity of the free space ε_0 and the dielectric displacement D. Doing further calculations and introducing the relative permittivity ε_r, also referred to as dielectric constant, yields the dielectric susceptibility x.

$$\varepsilon_r = \frac{\varepsilon}{\varepsilon_0} \qquad (6)$$

$$P = \varepsilon_0 \varepsilon_r E - \varepsilon_0 E = xE \qquad (7)$$

In addition to hysteresis loops also plots of the permittivity ε_{deriv} versus the electric field E can be used to characterize linear or non-linear dielectrics. ε_{deriv} is calculated as follows:

$$\varepsilon_{deriv} = \frac{\partial P}{\partial E} \times \frac{1}{\varepsilon_0} \qquad (8)$$

Here linear dielectrics show no change of ε_{deriv}, while non-linear dielectrics react depending on the field applied.

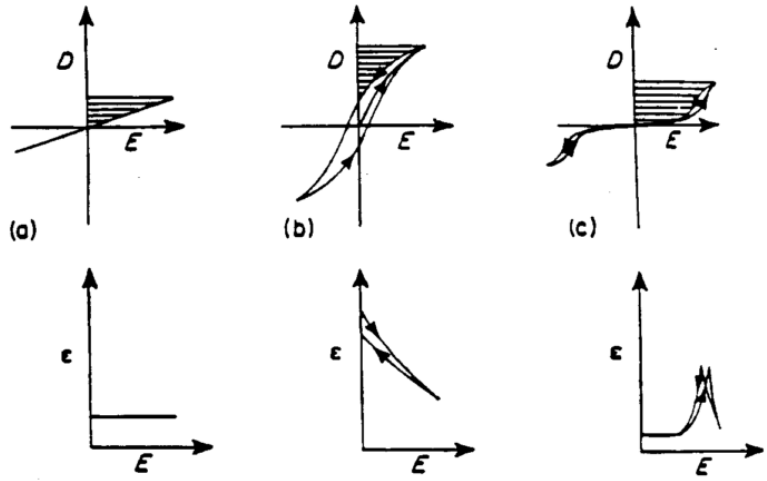

Figure 4: Hysteresis loops of a) linear dielectric, and non-linear dielectrics b) ferroelectric and c) antiferroelectric material, with corresponding permittivity ε_{deriv} vs electric field E [3]

The dark area between the y-axis and the hysteresis loop denotes the recoverable energy, while the area inside the loop labels the energy lost during the process ΔE. This energy is mostly lost as heat or acoustic waves.

Linear dielectrics are often used as insulating material since they often obtain a high dielectric breakdown field. Non-linear dielectrics are mostly ferroelectric or antiferroelectric materials, such as ceramics or sometimes polymers. Unlike ferroelectics, which have a non-zero dipole moment at zero field, anti-ferroelectics possess dipole moments opposing each other and thus yielding a net-zero polarization. The applied field where the anti-ferroelectic behavior is converted to a ferroelectric one is called the switching field, this allows the accumulation of an additional amount of energy.

2.2.1 Ferroelectricity

As already discussed before, ferroelectrics possess a non-centrosymmetric crystal structure and hence are polar, the orientation of the polarization can be readjusted by an applied electric field of sufficient magnitude. This polarization can be removed by raising the temperature above a critical value, the so called Curie-Temperature T_c, where the material will be paraelectric. The relative permittivity often reaches a maximum around this transition temperature and also the crystals long- and short-range orders often rearrange. [5]

One has to distinguish between three ways in how these rearrangements can take place:

1) Phase transitions of first order, where a sudden change in the crystals structure takes place, this is accompanied by a change in the volume. Here a specific amount of energy (heat of transformation) is consumed or released.
2) Phase transitions of second order, where a continuous change in the structure takes place, this can be accompanied by sudden changes in related properties. [5]
3) Diffuse phase transition, which doesn't occur at a definite temperature or field but gradually over a broader range. [6]

Barium titanate is one of the stereotype ferroelectric ceramics, its paraelectric-to-ferroelectric transition upon cooling to T_c is of first order, attended by a structural change from cubic to tetragonal phase. Also typical for this kind of transition is a hysteretic effect. [7]

There are three basic mechanisms for the formation of a spontaneous polarization:

1) Displacive ferroelectrics: when leaving the paraelectric phase two sublattices are shifted against each other, here dipoles are being created
2) Order-disorder ferroelectrics: while heating, the order of the dipoles at the transition point is being lost, but the dipoles itself do not vanish. During cooling the randomly located ions of the paraelectric phase start to align themselves again when reaching the polar phase.
3) Combined type: most materials are of the combined type [8]

Many ferroelectrics such as Barium titanate furthermore possess a perovskite crystal structure (ABO_3). To predict a good fit of the ions in the structure, the following relation can be taken into account:

$$R_A + R_O = 2(R_B + R_O) \qquad (9)$$

R_A, R_B and R_O represent the ionic radius of the cations and the oxygen respectively.

2.2.1.1 Phase Stability

This leads to Goldschmidt's tolerance factor for perovskite structures, which averages out at values around 0,95 < t< 1,06. The aberration of the ideal value of t = 1 results from small lattice shifts due to the limitation of energy.

$$t = \frac{(R_A + R_O)}{\sqrt{2}\,(R_B + R_O)} \quad (1)$$

A problem occurring when only taking ionic radii into account is the fact, that also polarizability and electron lone pairs (such as in Pb^{2+}) account for the stability of a structure.

For example the AFE behavior in $PbZrO_3$ (PZ) is supported by the lead ions therefore substituting them either by isovalent or aliovalent ions will change the materials properties. The lone pair electrons of the Pb cations e.g. are responsible for the strong local polarization. Larger substituents such as Ba^{2+} are stabilizing the FE phase whilst smaller substituents e.g. Sr^{2+} and Ca^{2+} induce an intermediate AFE state. Furthermore the substitution of Zr^{4+} by Ti^{4+} leads to the formation of $Pb(Zr_xTi_{1-x})O_3$, also referred to as PZT, and an additional FE phase between the PE and AFE state. [9] This is due to the fact that bigger ions occupying the B-site (t<1) favor the formation of orthorhombic or rhombohedra like structures, hence allowing AFE polarization, whilst smaller B-ions favor tetragonal structures giving rise to ferroelectric phases.

For PZT at a rate of substitution where x ≈ 0,45, the so called morphotropic phase boundary, two ferroelectric phases, differing in their structure, can coexist. [3]

2.2.2 Antiferroelectricity

Having two polar sublattices opposing each other, antiferroelectric materials have a zero net-polarization. By applying an electric field of sufficient magnitude, an anti-ferroelectric can be switched to a ferroelectric state, the field needed is called the switching field E_{switch}.

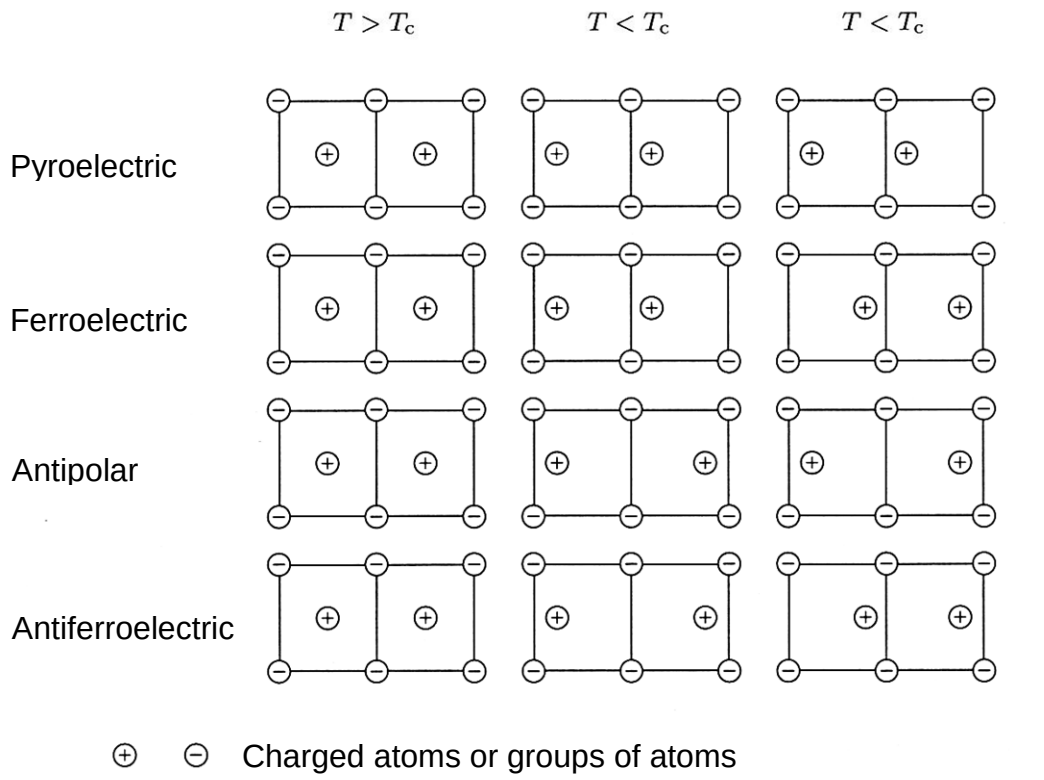

Figure 5: Polarization mechanisms [4]

Antiferroelectrics have a typical double hysteresis loop that can be seen in Figure 4c. Smolenskii ([3], Smolenskii (1984) therein) postulated, FE-AFE phase transitions will occur as function of temperature, pressure and electric field. Those transitions are often accompanied with a change in polarization or mechanical strain. A antiferroelectric-to-paraelectric phase transition will take place above the Neel-Temperature. [3]

Especially the perovskite structure tends to allow rearrangements that differ only slightly in their energy.

2.2.2.1 Antiferroelectric Materials [9]

The class of AFE materials is not only subject to a significant scientific interest because of their electrical properties but also for their technological applications including high-energy storage, actuators or transducers.

The group of antiferroelectrics includes among others liquid crystals, hydrogen-bonded materials, such as ice or potassium dihydrogen phosphate, as well as ceramics featuring perovskite-like structure like sodium niobate or lead zirconate.

2.2.2.1.1 Lead zirconate

Lead zirconate, $PbZrO_3$, as one of the standard antiferroelectric materials is in its low temperature phase of orthorhombic symmetry ([9], Ref. [7] therein), thus enabling 60°, 90° and 180° domains. At elevated temperatures a transition to a cubic structure with paraelectric behavior occurs, between those two phases a ferroelectric rhombohedral phase was discovered ([9], Ref. [25, 30, 36-38] therein). Due to these phase changes a possibility to modify or stabilize either of those phases via variations in the chemical composition needs to be explored.

The lead ions were found to be shifted along the cubic [110] directions, resulting in the AFE behavior. Hence they often are substituted by isovalent or aliovalent ions, like alkaline-earth metals or lanthanides respectively. Another possible substitution takes place on the perovskites B-site, where e.g. Ti^{4+} replaces Zr^{4+}.

2.3 The System PZT

PZT, lead zirconate titanate, a solid solution with the general formula $Pb(Zr_{1-x}Ti_x)O_3$ is one of the most studied dielectricmaterials. Especially the composition around the morphotropic phase boundary with its distinct electromechanical properties gives rise to a strong scientific interest. The morphotropic phase boundary as seen today is not a sharp line separating the high temperature rhombohedral from the tetragonal phase but a diffuse zone that also shows a temperature-dependence in compositional range with a mixture of monoclinic and tetragonal phases.

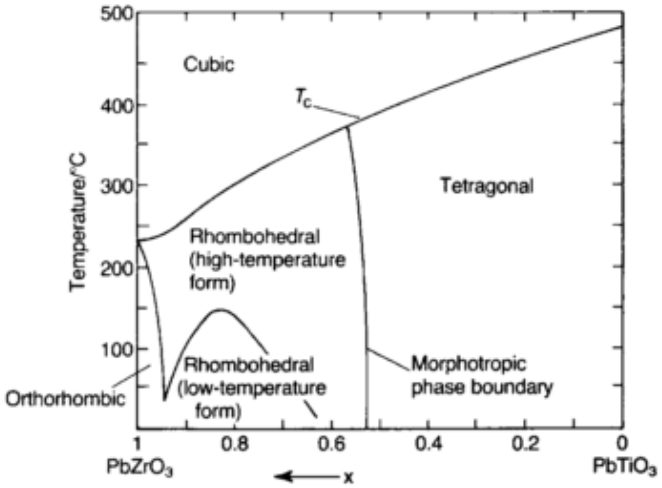

Figure 6: Phase diagram of the PZT system [1] (see Ref. [1] therein)

2.3.1 Influence of Substituents

While isovalent ions, such as barium, substituting lead on the A-site may have an influence on the polar ordering due to the absence of the lone-pair effect [9], aliovalent ions induce vacancies.

By replacing lead with a donor substituent, cation vacancies are introduced, while acceptor substituents are compensated by oxygen vacancies. In contrast to oxygen ions, which form a continuous lattice, cations and cation vacancies have to overcome a higher energy barrier in order to interchange and hence the mobility is much lower.

An ion and its vacancy form a dipolar pair where donor-cation combinations seem to have a more stable orientation than the oxygen-acceptor pair. A reorientation can occur under an electric field and elevated temperature.

Table 1 shows a small selection of possible substituents for the PZT system.

Table 1: some aliovalent substituents either for A- or B-site

A-site	Donor	La^{3+}, Bi^{3+}, Nd^{3+}
	Acceptor	Nb^{5+}, Ta^{5+}, Sb^{5+}
B-site	Donor	K^{+}, Rb^{+}
	Acceptor	Co^{3+}, Fe^{3+}, Cu^{3+}

Whilst introducing acceptors to PZT will lead to a decrease in the size of the unit cell, donors will reduce oxygen vacancies and therefore give rise to wall movements by destabilizing domains. In the course of donor doping also an increase in e.g. permittivity and dielectric losses can be found.

2.3.1.1 Lanthanum as Dopant for PZT

Lanthanum as a common donor dopant for PZT causes a charge compensation mechanism resulting it the formation of mostly A-site vacancies but also a small influence on B-site vacancies is possible. The likelihood of the appearance of vacancies on either sites can be influences by the lanthanum content and the amount of lead atoms substituted. [10, 11] Also lanthanum's ionic radius can affect the site where vacancies are introduced. [12] If La^{3+} only substitutes on the A-site it replaces one and a half Pb^{2+}-ions, resulting in the following formula.

$$Pb_{1-1,5a}La_a(Zr_{1-x}Ti_x)O_3 \quad (10)$$

However, heavy doping with lanthanum requests the incorporation of a lead elimination parameter α. [13]

$$Pb_{1-\propto a}La_a(Zr_{1-x}Ti_x)O_{3+a(1,5-\propto)} \quad (11)$$

The lanthanum ions help to raise the resistivity therefore PLZT became one of the preferred dielectric materials for ceramic capacitors. [14] Already an amount of 2,5 % lanthanum in PZT lowers the electrical conductivity on average to about 1000 times those of pure PZT and raises the dielectric constant 2- to 3-fold. [13]

2.4 Processing PLZT

Unless otherwise noted, the following part is an excerpt of “Ceramic Processing” by M. N. Rahaman, see Ref. [15].

Beside dopants also the microstructure and hence the processing method have a strong influence on the dielectric properties of a PLZT ceramic. In the following a deeper insight into these topics shall be given but since an introduction into ceramic processing in general would reach to far, the focus will be held especially on the methods used for this work.

The basic way for producing a polycrystalline ceramic from powders is indicated in Figure 7.

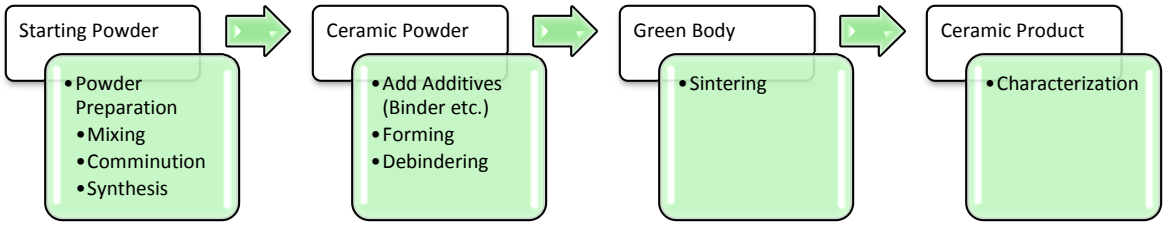

Figure 7: basic flowchart for the production of a ceramic body

2.4.1 Powder Preparation

Advanced ceramics must meet high quality standards and specific properties, often related to their microstructure and chemical composition, therefore the production process already starts with the preparation of the starting powders.

In order to reach a dense and well defined sintered body, important characteristics for the starting powders are:

- Chemical composition and impurity control: Since the chemical composition strongly affects the materials properties, a high degree of purity is necessary.
- Grain size and size distribution: The particle size has a strong effect on the sintering behavior, small particles enable dense products. A powder with a broad particle size distribution might lead to a better packing when pressing but it affects the microstructural development during sintering.

- Shape: Spherical particles allow a better control of the homogeneity of the packing.
- State of agglomeration: Agglomerates are clusters of homogenous chemical composition, which lead to difficulties in sintering and an over-all inhomogeneous chemical distribution.

2.4.1.1 Comminution

For creating a homogeneous composition in either ways chemical and by grain size, milling is the most frequently used process. There are three basic types:

1) High Compression Roller Mills are using compression forces to stress the material in between two rollers.
2) Jet Mills are crashing the grains via high impact forces produced by a jet stream of carrier gas.
3) Ball Mills use a combination of compression and impact forces to comminute grains.

2.4.2 Synthesis

The various methods to synthesize ceramic powders from starting powders can be separated into three basic categories:

1) Solid-state reactions normally take place in the way of mixed powdery reactants are being heated to produce a new solid product.
2) Synthesis from liquid solutions occurs by the formation of small nuclei and further growth by addition of more material to the surface, by evaporation of the liquid and nucleation and grain growth in a carrier gas or via the gel route where during drying a network is established.
3) Vapor-phase reactions where gaseous components react forming a solid.

2.4.2.1 Solid State Reactions

The reaction between solids, involving their decomposition, is also referred to as calcination. The first step in the reaction is always the decomposition of the starting powders. This step is followed by the actual chemical reaction between the solids. The educts A and B are forming the product C which also serves as the transport layer until the reaction is finished.

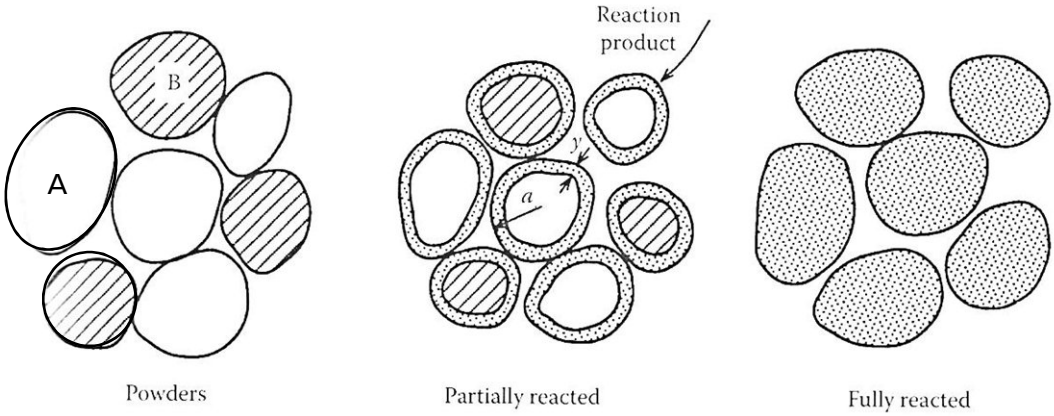

Figure 8: Schematic illustration of a solid-state reaction [15]

Due to the nature of the reaction well mixed compositions are needed in order to get homogeneous powders. Sometimes a second milling and calcination step is necessary to obtain a homogeneous product. A milling step after the completed calcination process is needed due to grain growth and the formation of agglomerates. Such a powder will be used for the subsequent forming processes to shape an adequate green body.

2.4.3 Sintering and Microstructural Development

The microstructure of a ceramic is highly depending on the process variables and it has a strong influence on the resulting properties. Also the quality of the starting materials and the compacting of the green body are of significant importance.

Generally advanced ceramics should obtain a small grain size, a high density and a possibly uniform microstructure. Since most ceramics are not single-phase a homogeneous distribution of the phases is desired.

2.4.3.1 Forming

In order to get ceramic products with a high density some further processing steps are actually necessary prior sintering.

1) Addition of additives: For advanced ceramics mostly organic compounds are used, since these can be removed from the ceramic by pyrolysis prior sintering. Depending on the forming method, different types of binders are used, f.e. solvents, dispersants, binders, plasticizers, lubricants etc.
2) Forming process: The following table will give a short overview of common techniques.

Table 2: Overview of forming techniques [15]

Forming Method	*Feed Material*	*Shape of Green Body*
Dry or Semidry Processing		
Die compaction	Powder or free-flowing granulates	Small, simple shape
Isostatic Pressing	Powder or fragile granules	Larger, more intricate shapes
Casting of a Slurry		
Slip casting	Free-flowing slurry with low binder content	Thin, intricate shapes
Tape casting	Free-flowing slurry with low binder content	Thin, sheets
Deformation of a Plastic Mass		
Extrusion	Moist mixture of powder and binder solution	Elongated shapes with uniform cross section
Injection molding	Granulated mixture of powder and solid binder	Small, intricate shapes

3) Pyrolysis/Debindering simply means an additive/binder burnout at intermediate temperatures to prevent the formation of cracks due to the decomposition and evaporation during the sintering process.

2.4.3.2 The Sintering Process

The actual heating process where, in the end, a dense ceramic body is obtained can be separated into two main categories:

1) Liquid-phase sintering: An adequate liquid phase assists the sintering process to produce high density specimen due to an improved material transport and better arrangement of the particles. Since the liquid phase wets all particles

there is a significant reduction of the vapor phase between the single grains, thus reducing pores.

2) Solid-state sintering: Heating the initial porous polycrystalline green body will first lead to the formation of necks followed by an ongoing neck growth and the evolution of grain boundaries. A network of open pores separates the joining grains. Further heating results in the elimination of open pores and the formation of a 3D-network. Depending on the density reached this grain network could be separated by a network of pores.

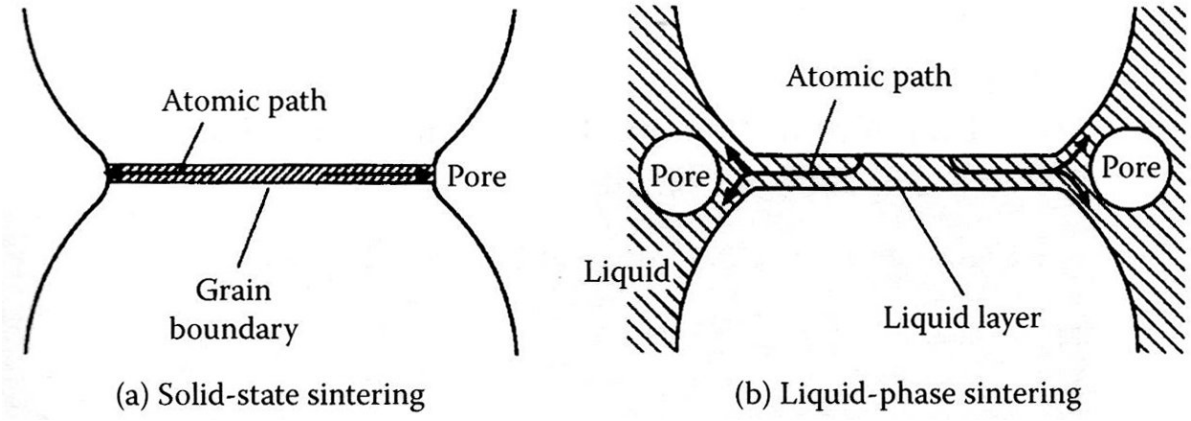

Figure 9: Idealized two-sphere model, showing differences in solid-state and liquid-phase sintering [15]

2.4.3.2.1 Solid State Sintering

Sintering, as it reduces vapor-solid interphases, goes along with a reduction in free surface energy which is seen as the driving force for this process. Since the free surface energy is a function of the particle radii, smaller particles have a higher impulsion in starting to sinter.

The surface free energy of a many-particle system can be written as

$$E_S = \frac{3\gamma_{SV}V_m}{a} \quad (12)$$

where γ_{SV} is the specific surface energy, V_m denotes the molar volume and a is the radius of the spherical particles.

Phase Boundaries

As already mentioned, during sintering, there is a decrease in surface free energy from reduction of pore surface areas but an increase in energy related to grain boundaries because of a growing grain boundary area. So grain boundary effects can be taken into account in order to predict if a pore is going to vanish or to grow during the heating. The following assumptions need to be made in order to predict if a pore will vanish or grow:

- The grains enclosing the pore have to have the same curvature everywhere around the pore.
- There also must be a zero-net force between the junction of grains and the pore.

Figure 10 shows a schematic of different ways a pore can be connected to its surrounding grains and how this affects its stability.

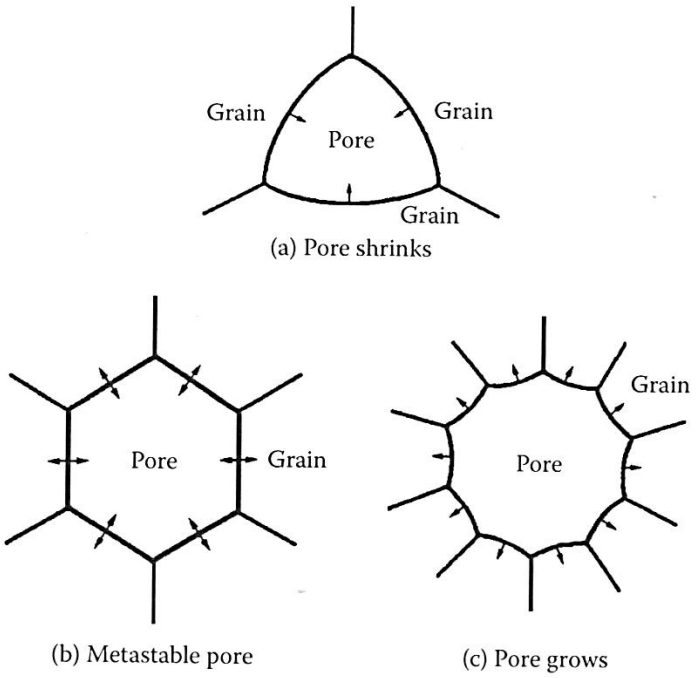

Figure 10: Pore stability depending on the pore coordination number [15]

So the stability of the can either be seen as dependent to the magnitudes of the surface free energy and the energy of the grain boundaries or through a geometrical point of view. When the pore is concave, it will shrink, when the pore is convex curved it will grow.

This can easily be explained via the following model:
Assuming a 2 D pore with grains creating an opening angle of 120° is surrounded by N grains where N is the coordination number of the pore. As seen in Figure 10, a pore with N<6 will possess concave sides and shrink, a pore with N>6 owns concave sides and grows while a pore with N=6 (critical number) is metastable and can either shrink or grow.

This model also shows why the grain size as well as the compaction of the green body is critical for a dense product.

Steps in the Sintering Process

There are several mechanisms leading to a bonding and growing together of particles:

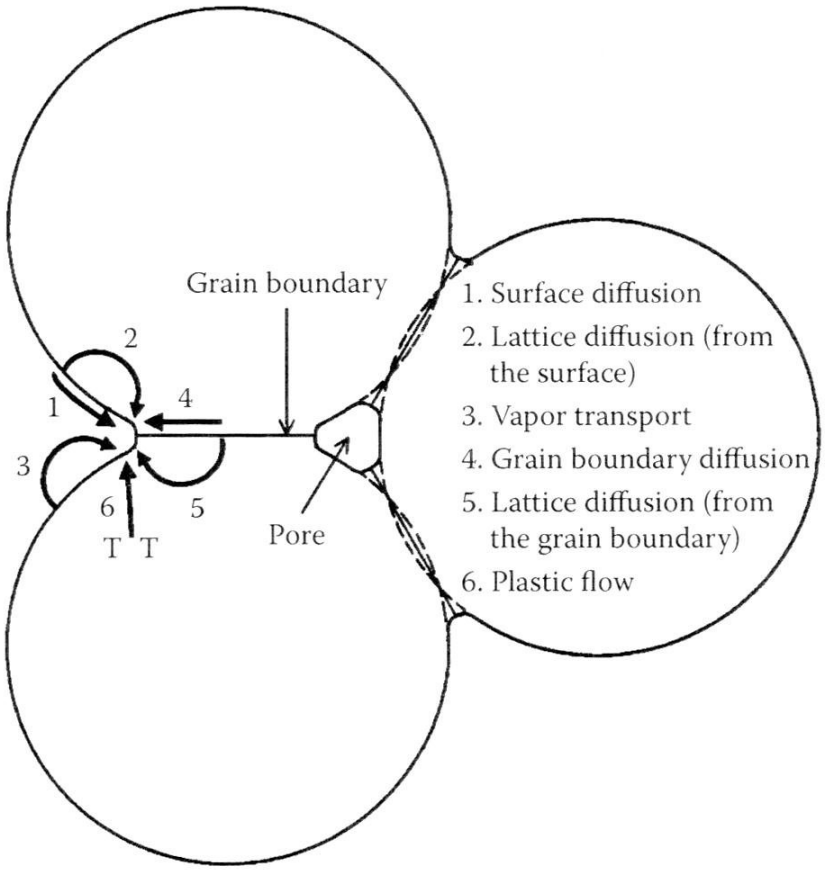

Figure 11: Sintering steps [15]

Steps 1, 2 and 3 are important for connecting the particles but they do not cause a densification but coarsening. However, steps 4 and 5 are seen as the most important ones when it comes to produce a dense polycrystalline ceramic. Step 6 allows further densification and additionally leads to neck growth but it is more associated with metals than ceramics.

In coarsening, the grain growth is accompanied by an increase in the pore sizes. It reduces the rate of sintering and leads to abnormal grains, e.g. very big or stretched ones besides small sized grains. Controlling the grain growth can be achieved by adding dopants.

2.4.3.2.2 Sintering of PLZT

Due to the rather low melting point of lead oxide (~850°C) in relation to usual sintering temperatures (>1000°C) evaporation of PbO is a crucial problem, leading to an uncontrollable composition and microstructure. Therefore PLZT samples are often supplemented with additional lead oxide and sintered in closed crucibles, embedded in lead oxide-containing atmospheric powder.

The excess of lead oxide is normally added during the powder preparation, the amount of additional lead varies from 1 % to 20 % in the literature, depending on the sintering technique. [16], [17],

As mentioned, the arrangement of crucibles can help to minimize the loss of lead during sintering, Figure 12 and Figure 13 show two possible ways:

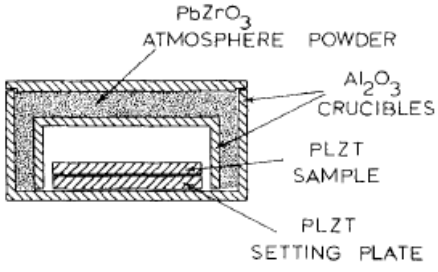

Figure 12: apparatus for sintering PLZT [16]

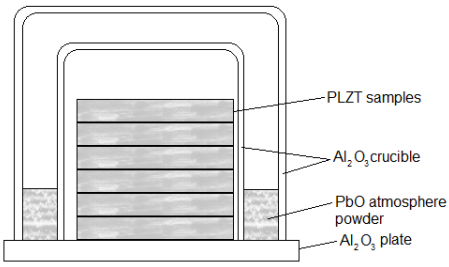

Figure 13: PLZT sintering arrangement

The excess of lead powder in the green body melts during the sintering leading to a change from solid-state into liquid-phase sintering. The liquid lead phase on one hand leads to a rapid densification, while on the other hand could inhibit grain growth due to a reduction of the driving force and an increased diffusion path for material transport. ([16], Reference [3] therein)

Affecting the Densification via an Excess of Lead Oxide [17]

In their studies, using PLZT (9/65/35), Song and Kim found, that already during calcination a significant amount of lead was lost. (0,7 % at 1000°C for 2h) They also found samples containing an excess of 2 % PbO had a highly uniform structure, in contrast, samples containing 7 % excess of lead had large pores. Specimen with a lead-deficiency of about 1 % had fine residual pores embedded in the grains (intragranular porosity). They also discovered a steady increase in density in the regime between 0 – 4 % excess PbO. This might be due to whether or not a liquid phase exists during the sintering process.

Evaporation of Lead [18]

The total amount of lead in a PZT (65/35) ceramic is 67 %, during the experiments Northrop could detect losses between 0,5 % and 61 %. It was found that the lead vaporization can be separated into two steps, first the vaporization of unreacted PbO with a logarithmic time dependent step, and second a diffusion-controlled, parabolic time-dependent step.

During the first step, at 575°C first losses could be detected, the weight loss was dependent only on the amount of material present; density, weight and configurations of pellets had no influence. The loss of PbO presumably takes place via pore diffusion. At temperatures above 900°C all unreacted PbO is lost.

The second step starts at temperatures around 780°C in a continuous weight loss yielding a white lead-depleted region (PZ phase) on the specimen’s surface. Here the weight loss was strongly affected by the geometry and thus the surface area of the samples. Northrop could also show an increase in the evaporation rate with cation vacancies by partial substitution of Pb with bismuth.

2.4.4 Defect Chemistry

Crystals generally contain two different types of defects [19]:

- Point defects
- Line defects

However, since point defects play a major role, they shall be discussed further. A possibility to describe them is the Kröger-Vink notation (for further explanations see [20]).

2.4.4.1 Defect Types

Frenkel and Schottky defects are among the most important intrinsic crystalline defects. While in ionic samples both, ionic and electronic defects can occur.

2.4.4.1.1 Frenkel Defects

When an atom occupies an interstitial site instead of its lattice site it leaves behind a vacancy. So Frenkel defects consist of a defect pair created by a lattice vacancy and a interstitial atom. Assuming a metal oxide, MO, this pair can be written as

$$M_M^X \underset{\rightarrow}{\leftarrow} M_i^{\bullet\bullet} + V_M'' \,. \quad (13)$$

2.4.4.1.2 Schottky Defects

Schottky defects only occur in ionic compounds, they classify a stoichiometric pair of cation and anion vacancies. For a metal oxide, this can be written as

$$M_M + O_O \underset{\leftarrow}{\rightarrow} V_M'' + V_O^{\bullet\bullet} + M_B + O_B. \quad (14)$$

B marks any place where a lattice can form (grain boundaries, dislocations, surfaces), so Schottky defects can create new lattice points.

2.4.4.1.3 Electronic Defects

In ceramics, above 0 K, intrinsic electronic disorder causes the formation of holes in the valence band and free electrons in the conduction band. The concentration of these defects is a function of the temperature and the band gap.

2.4.4.1.4 Defect Formation

The concentration of point defects in ceramics is a function of the dopant concentration. For predicting the defect concentration, defect chemical reactions are used. Prior some important principles have to be taken into account:

1) The mass action law has to be fulfilled.
2) The charges must be balanced at either side in such a way that electrical neutrality is achieved.
3) The cation to anion ratio mustn't be changed, even though lattice sites may be created or in the case of non-stoichiometry.

Example: Assuming a L_2O_3 dopand added to a MO compound and a reaction of MO with oxygen.

$$\frac{1}{2}O_2 \rightarrow O_O^X + V_M'' + 2h^\bullet \qquad (15)$$

Considering all L atoms occupy M sites in the lattice as donors:

$$L_2O_3 \xrightarrow{MO} 2L_M^\bullet + V_M'' + 3O_O^x \qquad (16)$$

3 Materials and Methods

In this section a short overview about the materials and methods used for this work shall be given.

3.1 Sample Processing

Figure 14 indicates the steps in the sample preparation process, which follows the Mixed Oxide Method. For more detailed information please see the following chapters.

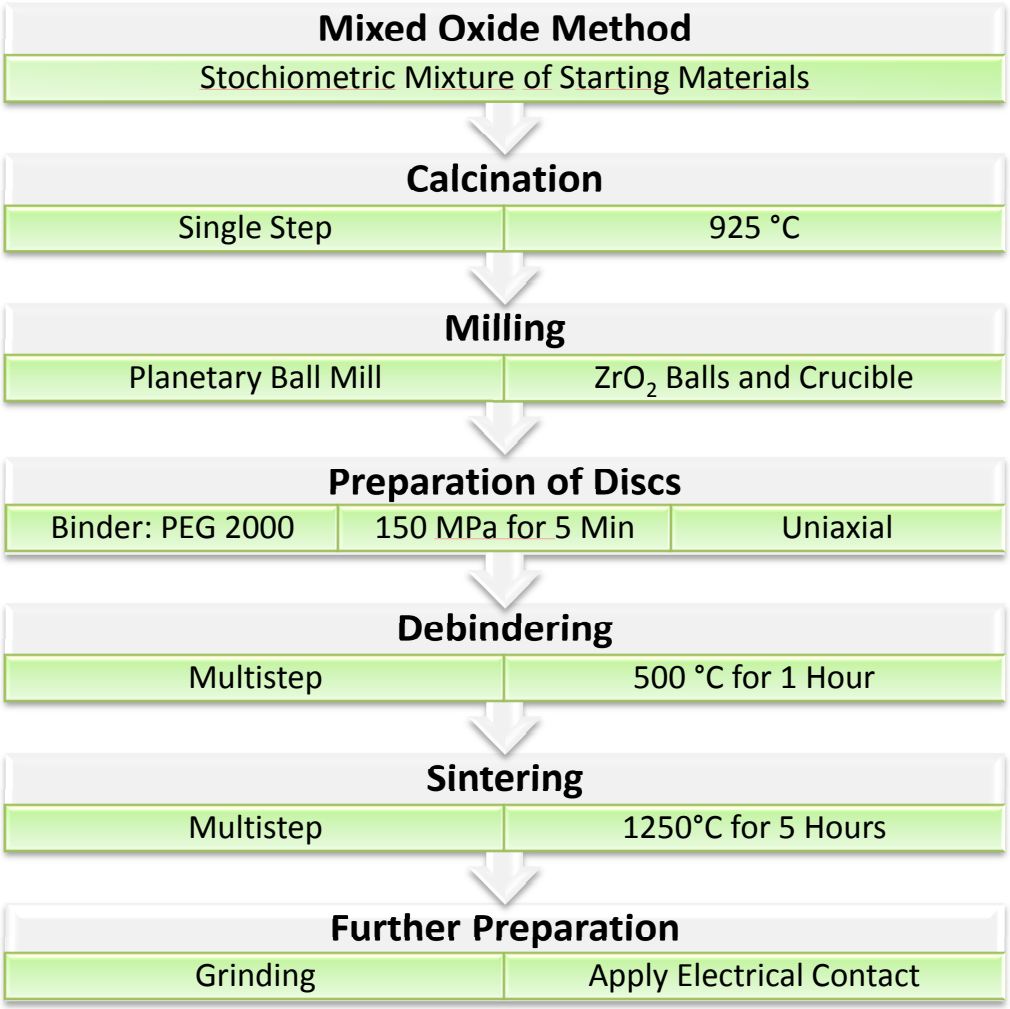

Figure 14: Steps in sample preparation

The aim was to produce two basic compositions of PLZT with differing Zr-/Ti-content mixed with varying concentrations of Ba, Ca and Sr according to the following

formula: $(Pb_{0,91-x-y-z}Ba_xCa_ySr_zLa_{0,06})(Zr_{1-m}Ti_m)O_3$ (x, y, z = 0 & 0,02, m = 0,10 & 0,15). Samples containing 90 % of Zirconium were designated “I90”, whilst those containing 85 % were labeled “M85”. Including the dopants in the sample names leads to a matrix of 16 samples as indicated in Table 3.

Table 3: Sample Matrix, stoichiometric quantities in %mol

Sample No.	Composition	Pb	La	Ca	Sr	Ba	Zr	Ti
1	I90	0,91	0,06	0	0	0	0,90	0,10
2	M85	0,91	0,06	0	0	0	0,85	0,15
3	I90_Ba	0,89	0,06	0	0	0,02	0,90	0,10
4	M85_Ba	0,89	0,06	0	0	0,02	0,85	0,15
5	I90_Sr	0,89	0,06	0	0,02	0	0,90	0,10
6	M85_Sr	0,89	0,06	0	0,02	0	0,85	0,15
7	I90_Ca	0,89	0,06	0,02	0	0	0,90	0,10
8	M85_Ca	0,89	0,06	0,02	0	0	0,85	0,15
9	I90_BaSr	0,87	0,06	0	0,02	0,02	0,90	0,10
10	M85_BaSr	0,87	0,06	0	0,02	0,02	0,85	0,15
11	I90_BaCa	0,87	0,06	0,02	0	0,02	0,90	0,10
12	M85_BaCa	0,87	0,06	0,02	0	0,02	0,85	0,15
13	I90_CaSr	0,87	0,06	0,02	0,02	0	0,90	0,10
14	M85_CaSr	0,87	0,06	0,02	0,02	0	0,85	0,15
15	I90_BaCaSr	0,85	0,06	0,02	0,02	0,02	0,90	0,10
16	M85_BaCaSr	0,85	0,06	0,02	0,02	0,02	0,85	0,15

3.2 Preparation of the Sample Powders

The sample powders were prepared by mixed-oxide method from:

- Titanium dioxide (99,8 %): Tronox Pigments, Holland BV
- Zirconium dioxide: MEL Chemicals, Manchester, UK
- Lead oxide (Pb_3O_4): Penox GmbH, Köln/Deutz, Deutschland
- Lanthanum oxide: Treibacher Industrie AG, Treibach, Österreich
- Calcium carbonate (High Purity CF 800): Solvay Bario e Derivati, Massa, Italy
- Barium carbonate: (Reagent Grade): Solvay Bario e Derivati, Massa, Italy
- Strontium carbonate: (Reagent Grade): Solvay Bario e Derivati, Massa, Italy

The starting materials were mixed according to the desired chemical composition of the samples, furthermore an excess of 2 % lead oxide was added to prevent lead deficiency. In order to homogenize the mixture prior calcination, it was milled in a planetary ball mill (Fritsch, classic line, Pulverisette 6) for 150 minutes using yttrium-stabilized zirconia vial and balls (5°mm) and distilled water as the liquid medium. After drying the powder mixtures at 100 °C they were sieved (test sieve, 500 µm) and calcined in a chamber furnace(Nabertherm N7H) in closed crucibles. Figure 15 shows the temperature program for the calcination step. It has to be noted that for all heating stages (calcination, debindering and sintering) the cooling rate deviates from the given plots due to the passive cooling used.

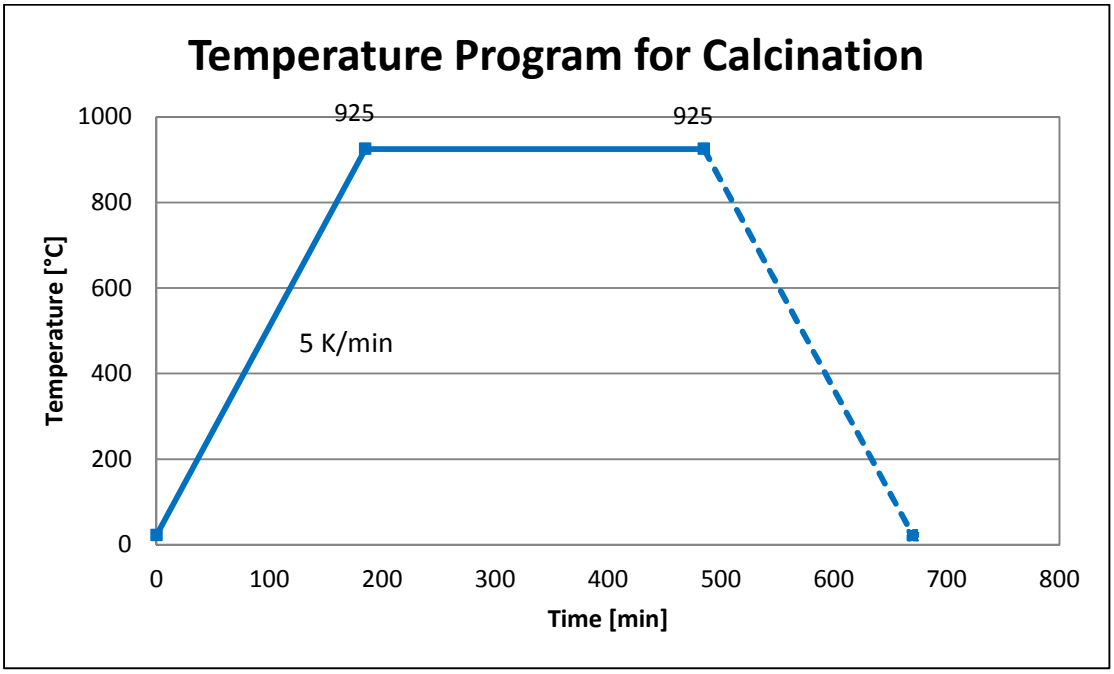

Figure 15: Temperature program for calcination, the dashed line indicates the natural cooling rate, 5 hours holding time at 925°C

3.3 Formation of the Green Bodies

For post-refining the product, a planetary mill (Fritsch Pulverisette 4), yttrium-stabilized zirconia vial and balls (2°mm) and distilled water were used, additionally a dispersant was added (Dispex A40, Ciba Spezialitätenchemie). The settings for this milling step were: 200 rpm, 5 x 20°minutes with a 10°minute break between the iterations. After, the powders were dried at 100°°C, sieved (180 µm) and mixed with 5°% polyethylene glycol (PEG20000; Alfa Aesar). The mixture was again dried

(80 °C) and sieved (180 µm). Finally the green bodies were pressed with a uniaxial pressure of 150 MPa for 5 minutes.

3.4 Sintering Experiments

Prior to sintering the debindering was carried out in a separate process at a maximum temperature of 500 °C with a multistep profile (Figure 17). As discussed in the previous chapter the sintering arrangement is crucial to prevent a high loss of lead in the samples and to maintain a proper lead-containing atmosphere. See Figure 16 for an illustration of the sample arrangement for the sintering stage.

Figure 16: Sintering arrangement

The experimental set-up and stacking of the green bodies is carried out based on the proposal of Snow [16]. To achieve high density ceramic products the sintering was carried out at a maximum temperature of 1250 °C as indicated in Figure 18.

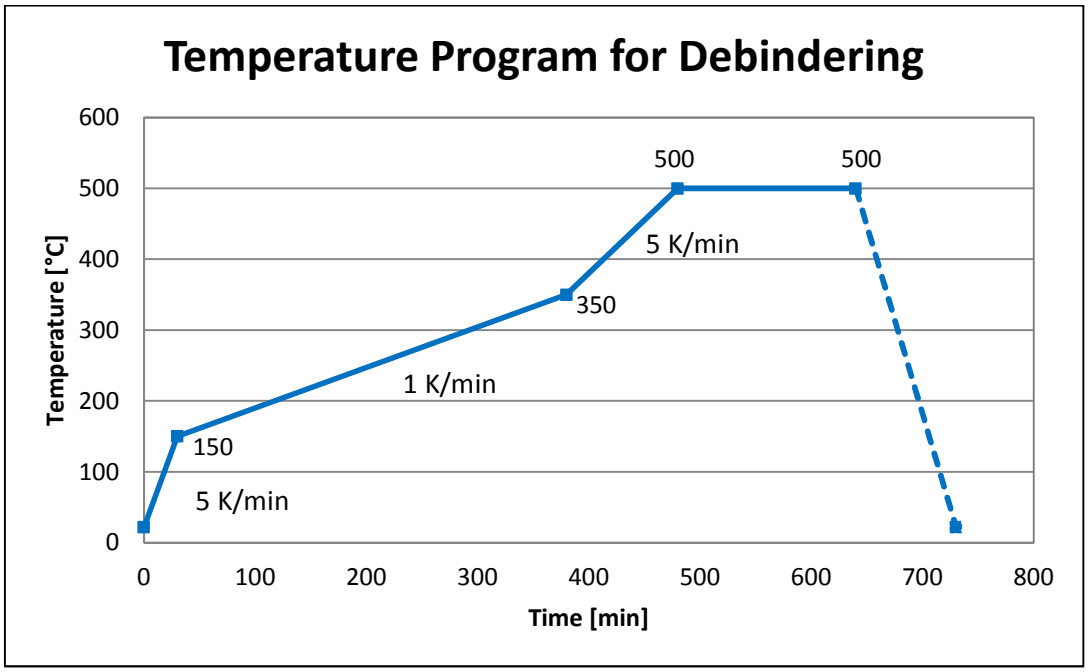

Figure 17: Temperature program for the debindering step, the dashed line indicates the natural cooling rate, 1 hour holding time at 500 °C

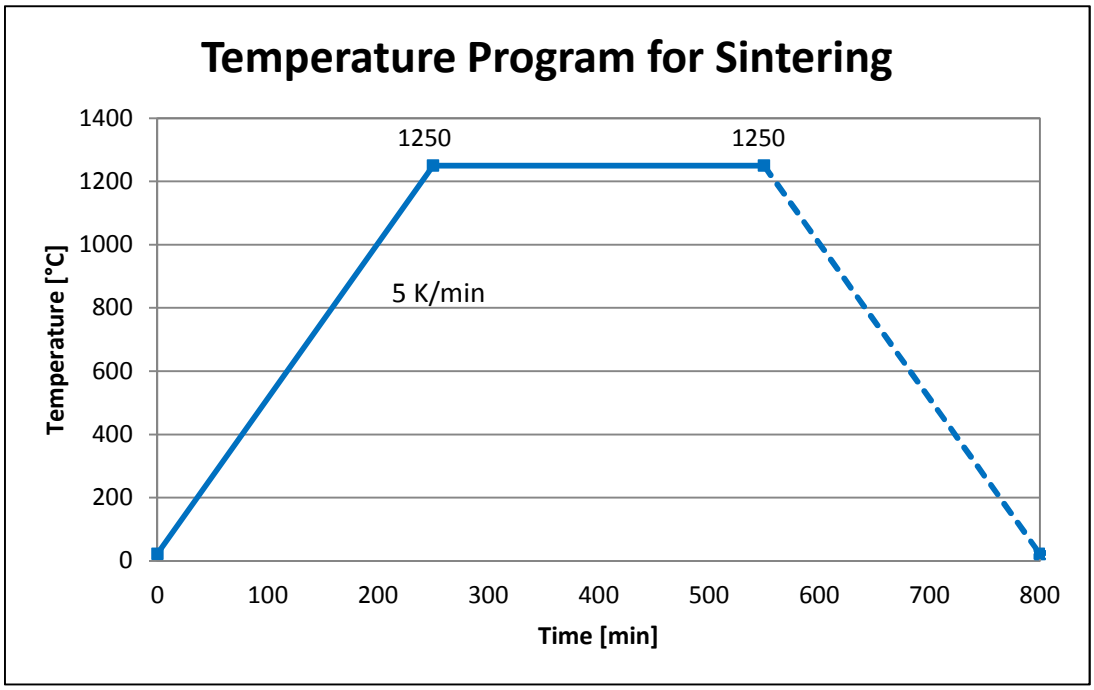

Figure 18: Temperature program for sintering, the dashed line indicates the natural cooling rate, 5 hours holding time at 1250 °C

3.4.1 Sinter Temperature and Dilatometric Analysis

The dilatometric analysis was carried out with a Netzsch DIL 420 C, in order to determine one sintering temperature suitable for all compositions.

For the Dilatometry the calcined powders after milling were pressed into cylinders of 330 mg, with a diameter of 5 mm and an average height of 2,5 – 3,3 mm. The force of 1 t was applied uniaxially for 20 seconds.

3.5 Sample Characterization

3.5.1 Calcination Weight Loss

For determining the weight loss upon calcination the crucibles and powders were weighted before and after the calcination process, the difference of these two masses was taken. For each composition a single value was obtained.

3.5.2 Density Studies

Two different methods were used to determine the density:

- Geometric density: From the sintered samples height and diameter were measured with a sliding caliper, for each value an average out of three measurements was taken. The mass of each disc divided by the volume calculated from those numbers make the geometric density.
- Density according to Archimedes' principle: the determination of the densities was carried out via an Archimedes scale where the sintered samples were weighted in air and immersed in a liquid (in this work distilled water). Via the weight difference due to bouyancy the density can be calculated.

For each composition eight samples were analyzed, the numbers in the diagrams are average numbers out of all these samples measured.

3.5.3 Shrinkage Studies

The shrinkage studies were carried out to verify the obtained density values and additionally control the sintering. For each composition eight samples were analyzed before and after the sintering stage using a sliding caliper. For every sample an average out of three measurements was taken for each dimension (diameter, height).

3.5.4 X-Ray Diffraction and Crystal Structure Analysis

θ/2θ measurements were done in order to control the calcination and sintering process using a Bruker AXS D5005 y-y (including a Cu-Kα emitter and a graphite secondary monochromator). The determination of the crystal structure and the calculation of the materials theoretic densities wer carried out via the Rietveld method using the X'Pert HighScore Plus 2.2.1 software package. Every composition was analyzed once.

3.5.5 Scanning Electron Microscopy

The SEM analysis were used to observe the influence of dopants on grain growth as well as the formation of secondary phases. For each material one sample was studied in the Zeiss Ultra 55 microscope.

- Secondary electrons have been detected for studies of the topography, e.g. pores and the grain network.
- Backscattered electrons were used to determine the homogenity of the material. This can be done due to the fact that heavier atoms have a higher backscattering cross-section and hence they show a more intense signal and can be detected as brighter spots on the image.
- Energy dispersive X-ray analysis were carried out for quantitative analysis of the materials stoichiometry. However due to interferences of the dopants (Ba, Ca, Sr) signals with the signals of the matrix (Pb, La, Zr, Ti) the concentration of the dopants could not be determined. Hence the results were used to give a rough overview of the phase distribution within the samples.
- The "Channeling Contrast Mode" [21] was used to determine the domain structure and orientation of the grains and subsequent the grain size distribution. This method makes use of the fact that differently oriented grains backscatter with different intensities.

3.5.6 Dielectric and Piezoelectric Properties

For the electric characterization silver paste as electric contact was applied on the samples. After this the samples were dried at 80 °C for 30 minutes and cooled down before surveying.

- Capacity and loss factor were determined with an impedance analyzer (HP 4192A LF Analyzer) at frequencies of 1 MHz and 10 MHz and a voltage of 1 V. The measurements were carried out before and after poling with the Fluke 1550B MegOhmMeter.
- The piezoelectric coefficient (d_{33}) was measured at a force of 0,25 N and a frequency of 110 Hz with the Piezotest PiezoMeter System PM300. The measuring was performed after poling of the samples.
- For the high-signal measurements the aixACCT aixPES system was used to record polarization versus electric field, polarization versus current and polarization versus strain loops. The voltage applied was dependent on the materials break-through voltage.

In the results one sample for each composition is being discussed.

4 Results

The aim of this work is to get an idea how alkaline earth metals influence the properties of PLZT, a second aspect was added due to problems with high loss of lead during processing. Hence the results were separated into three main parts. In the first part the pretests were discussed, here the objective was to control if there is a connection between the ionic radii and the masses on the A-side with the dielectric properties e.g. the switching field as discussed in the last part. This would enable to make further statements about the properties of a broader range of materials. The second part of the chapter will deal with the findings during the calcination and sintering steps while the third part will focus on the electric characterization of the material.

4.1 Pretesting

During the pretesting calculations regarding the crystal structure were carried out, the results were compared to find possible connections between them. This would allow making predictions for the behavior of similarly modified materials.

4.1.1 Effective Mass vs. Tolerance Factor

In the following diagram the connection between the Goldschmidt's tolerance factor and the effective mass at the A-site is shown. The calculation of the tolerance factor was done by separately calculating the average ionic radii of the A- and B- site ions of the perovskite lattice and then inserting the yielded numbers into equation

$$t = \frac{(R_A + R_O)}{\sqrt{2}\,(R_B + R_O)} \qquad (1).$$

For the effective mass of the A-site ions, weighted average values of the present ions were calculated.

The dots are creating a raster pattern, with the M85 compositions showing a higher Goldschmidt factor than the I90 mixtures.

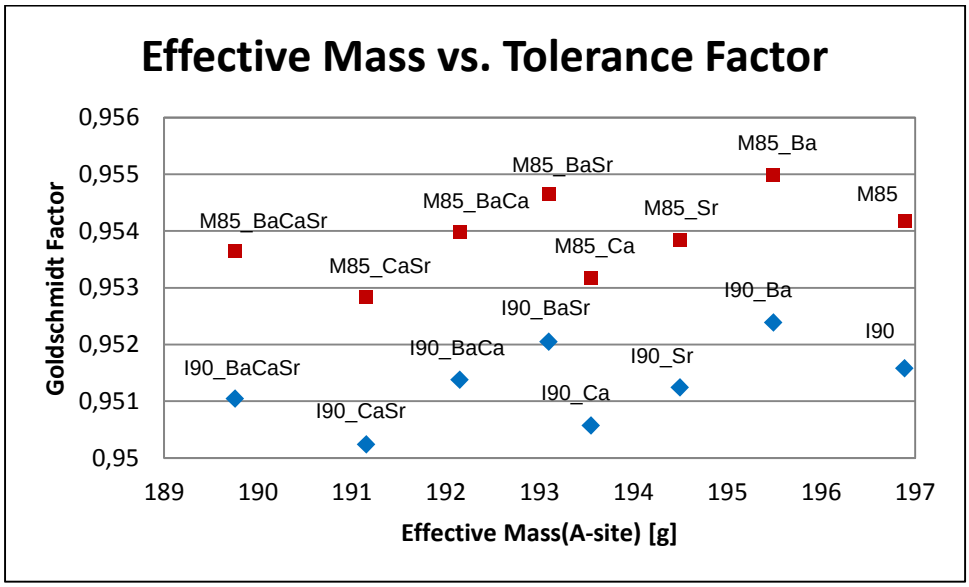

Figure 19: Effective mass vs. tolerance factor, the blue dots indicating mixtures of the I90 (PLZT (6/90/10)), the red dots indicating the M85 (PLZT (6/85/15)) compositions

4.1.2 Dilatometry

Figure 20 shows the loops obtained during the dilatometric analysis of the I90 mixtures. Between 778,4 °C and 846,4 °C the free lead oxide in the sample starts to melt, forming a liquid phase. At around 1100 °C the samples start to sinter.

Table 4: Sinter temperatures for selected I90 compositions

Composition	Dopants	Sintering Onset[°C]
I90 PLZT (6/90/10)	Ba	1122,4
	Sr	1086,6
	Ca	1129,2
	Ba, Sr, Ca	1138,2

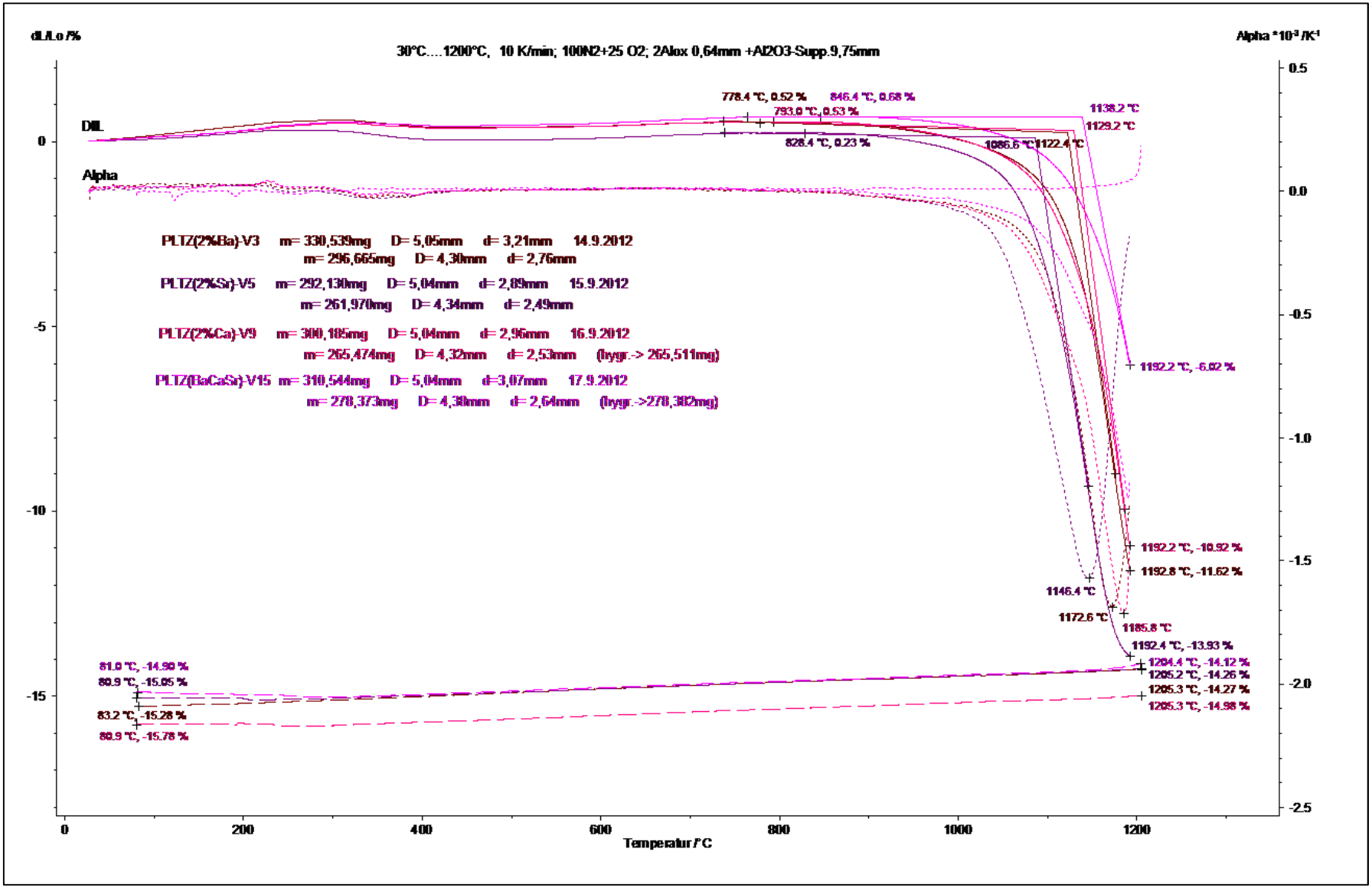

Figure 20: Dilatometric analysis of the single and fully doped sample powders of the I90 compositions

4.2 Measurements for Process Control

4.2.1 Calcination Weight Loss

In order to control the loss of lead oxide during calcination, weight loss studies were carried out. For the calculations it was assumed that the measured weight loss was solely due to the dissociation of Pb_3O_4 and further vaporization of lead oxide according to the following formula:

$$Pb_3O_4 \rightarrow PbO + O_2 \uparrow \qquad (17)$$

For the calculations of the weight loss, the measured total weight loss was corrected by the weight of the evaporating oxygen due to the dissociation reaction itself thus yielding the weight of the vaporized lead oxide only. As mentioned previously, a 2 % excess of lead oxide was added to account for the expected weight loss, which, as Figure 21 shows, proved to be necessary.

A clear dependence of dopant concentration on the weight loss can be observed, whereas the zirconium titanium ratio doesn't seem to have an influence on the results. The lowest weight loss can be found in the non-doped samples while the fully doped ones showed the highest losses.

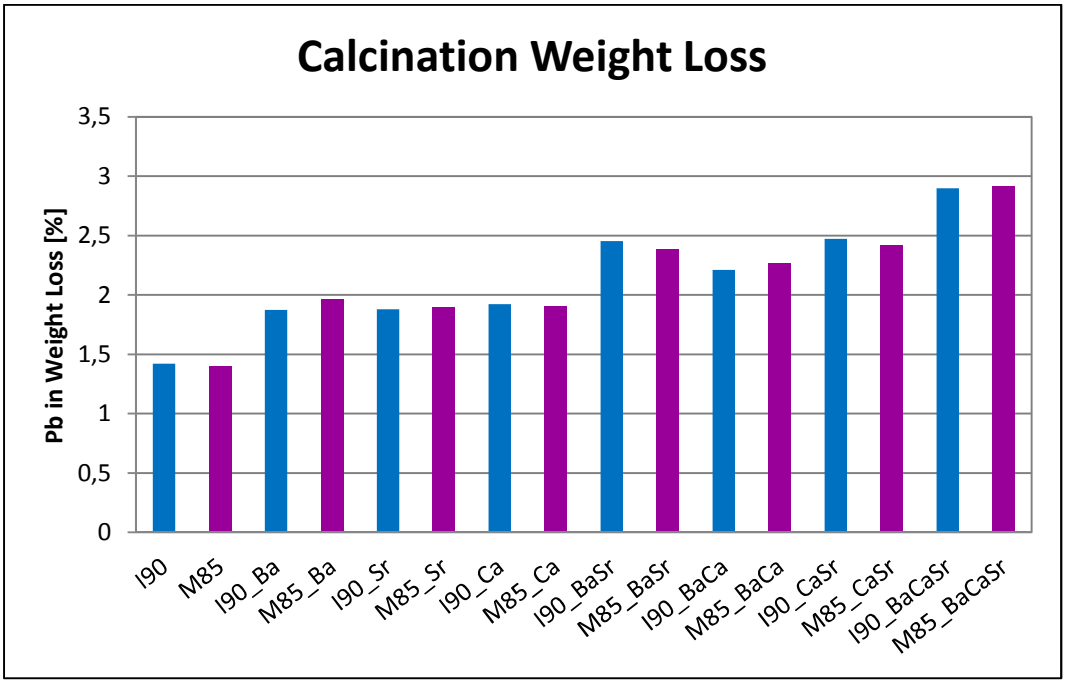

Figure 21: Weight loss after calcination, the loss occurring due to the evaporation of oxygen is already subtracted (see Equation (17))

4.2.2 Influence of Sinter Beddings on the Density

Measuring the density is a way to control the sintering. Due to this fact, for testing different sinter designs and atmosphere powders, the apparent densities of the sample discs were analyzed. All samples consisted of the PLZT (6/90/10) composition. Figure 22 shows the average weight loss within the sample stacks for different sinter beddings. For the calculation of the weight loss it was assumed that the loss was solely due to the evaporation of lead oxide, the dissociation reaction as discussed in the previous chapter was not taken into account. The loss was calculated from the initial weight of the sample less the weight after sintering. Due to the balanced densities and the relatively low weight loss non calcined lead zirconate was chosen for further sintering experiments as atmosphere powder.

Also as a result of the sintering design, a density gradient was expected within the sample stack. Whereas during the first sintering experiments, where the sample discs where put next to each other or a slit underneath the crucibles was held open, a strong gradient could be detected, it leveled off for the final sinter design where the slit was closed (compare Figure 23).

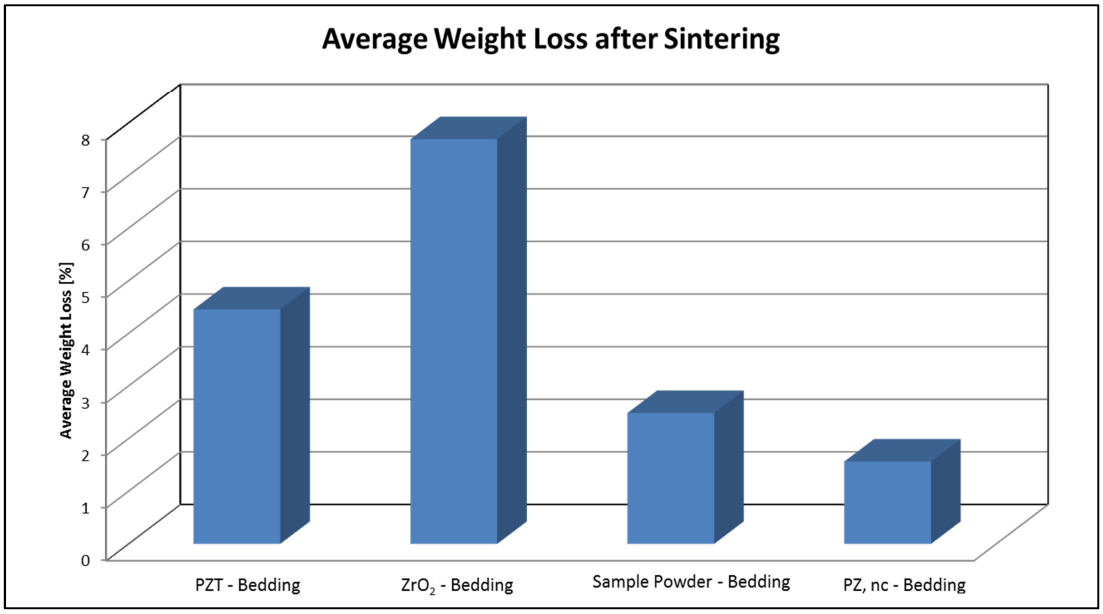

Figure 22: Average weight loss (out of 6 discs) of sintered I90 samples with different atmosphere powders (PZT…lead zirconate-titanate, PZ…lead zirconate, nc…non calcined lead zirconate)

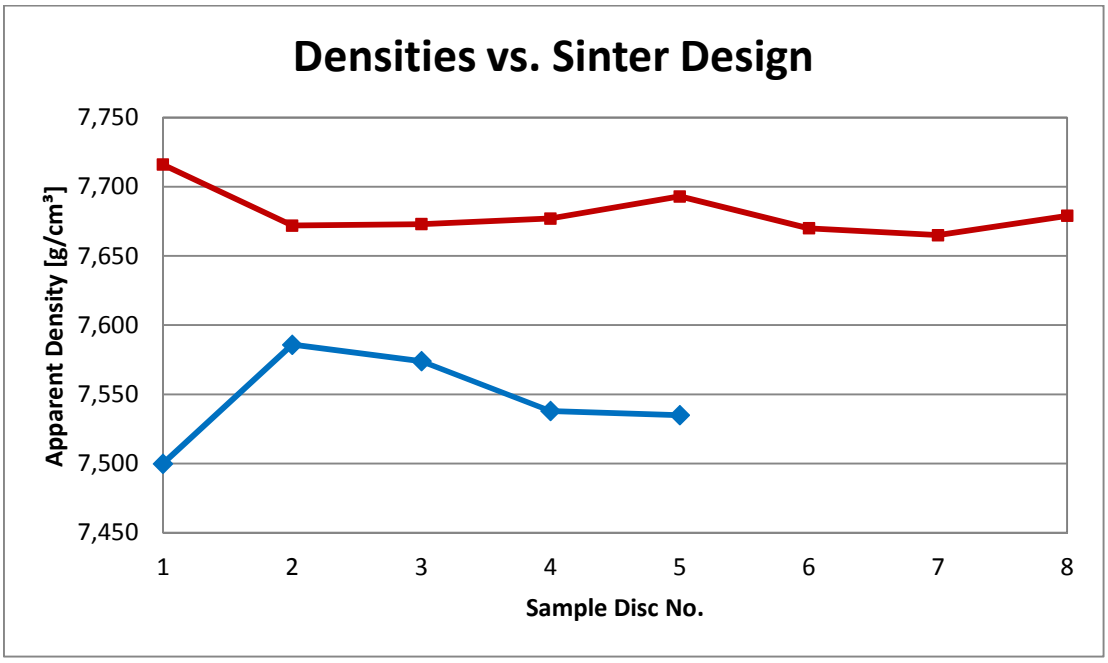

Figure 23: Density gradient of I90 samples with respect to the sinter design used, the blue line indicates a sinter design where a slit was held open underneath the crucibles whereas the slit was closed during the final sinter design (red line)

4.2.3 X-Ray Diffraction Analysis

To control the formation of the desired perovskite structure, XRD analyses were done after calcination and after the sintering step. One can clearly see the perovskite main peak at 30° in all spectra. (Figure 24 and Figure 26) It also can be observed that the peaks narrowed after the sintering step (Figure 25 and Figure 27), which is due to a higher degree of crystallinity. For all compositions a hexagonal crystal system was used for refining.

The spectra give no indication of secondary phases, this however might be due to the used refinement data since calculations showed significant deviations in the theoretic densities calculated and given by the software. Table 5 (see Appendix) gives an overview of the obtained values.

The values for the theoretic densities ρ were calculated with the following equation:

$$\rho_{theo} = \frac{Z*M}{N_A*V} * 10^{24} \quad (18)$$

where Z is the number of formula units in the unit cell, M the molar mass of the composition, N_A the Avogadro number and V the volume of the unit cell.

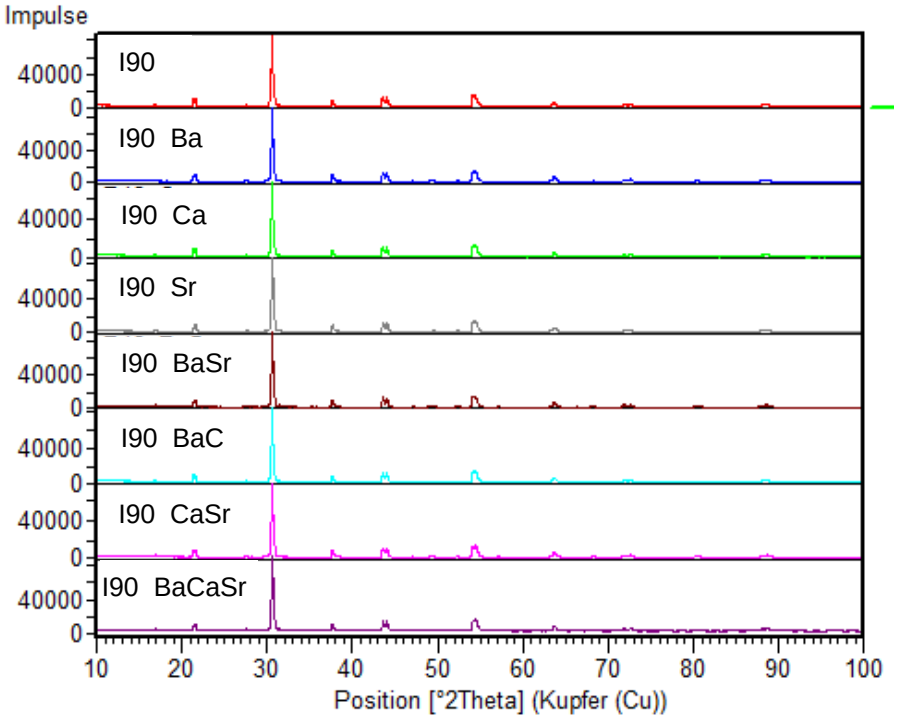

Figure 24: XRD-Spectra of I90 composition after calcination, one can clearly see the perovskite main peak at ~30°

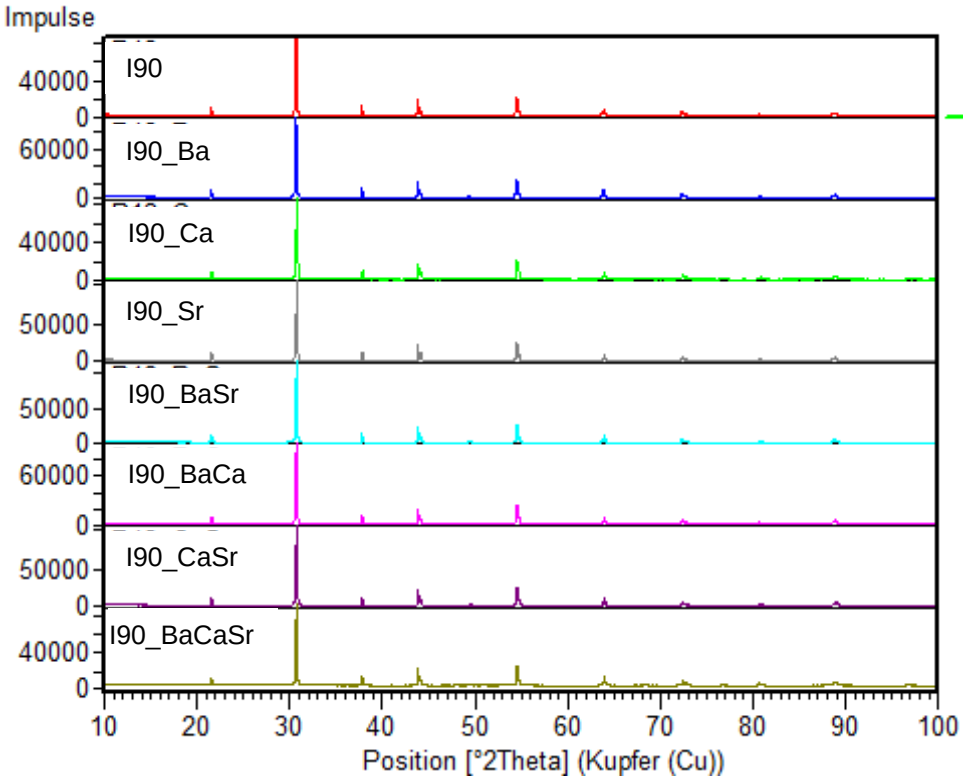

Figure 25: XRD spectra of I90 after the sintering step, more narrow peaks can be observed

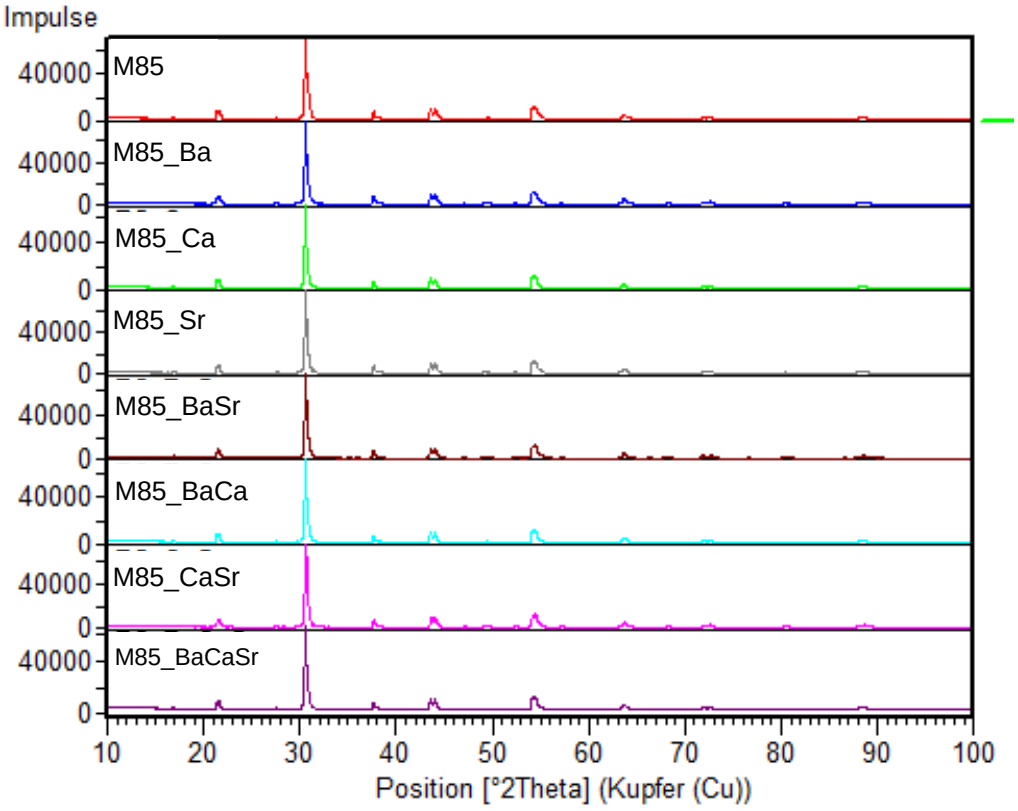

Figure 26: XRD spectra of the M85 composition after calcination with the perovskite main peak at ~30°

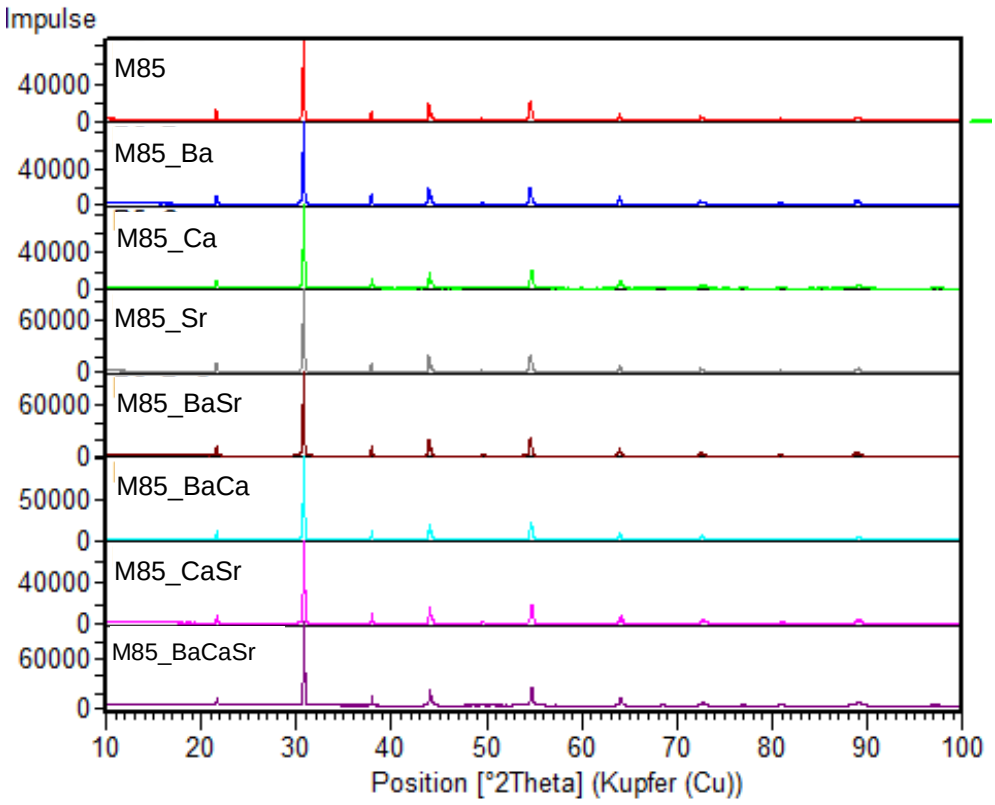

Figure 27: XRD spectra of M85 compositions after sintering

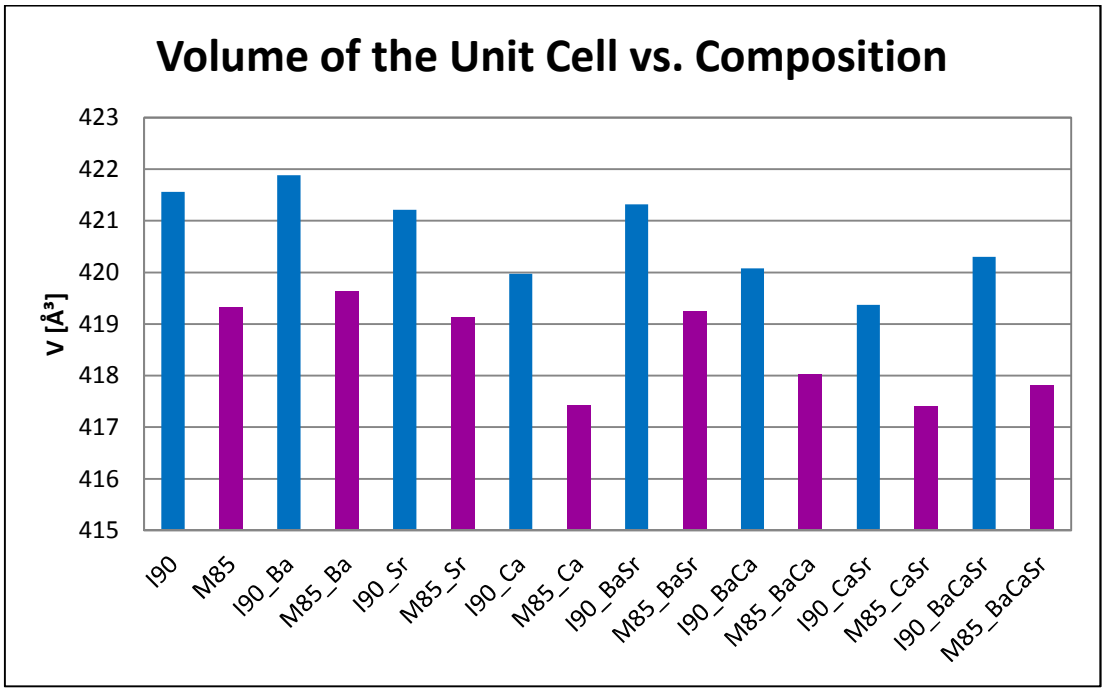

Figure 28: Comparison of the volume of the unit cell and the composition of the sintered samples

The changes of the volume of the unit cell agree with the changes of average ionic radii and indicate the substitution of Pb by the alkaline earth ions. This effect was also found by Ramam and Miguel. [22]

4.2.4 Densities of the Sintered Samples

A clear influence of the dopants on the relative densities can be seen. The relative density is calculated as follows:

$$\text{Relative Densitiy} = \frac{\text{Apparent Density}}{\text{Theoretical Density}} * 100 \qquad (19)$$

Where the apparent density is yielded via the Archimedes method and the theoretical density is taken from the XRD data.

Looking at the non-doped and single-doped samples the I90 compositions always possess higher densities than the M85 samples. With increasing dopant concentration the densities of PLZT (6/90/10) and PLZT (6/85/15) are assimilating. While there is a difference in the relative density of the non-doped samples of 2,6 %, for the fully doped mixtures is was reduced to 0,3 %. Additionally, the density of those fully doped samples is about 4,5 % lower for the I90 and 2,3 % lower for the M85

mixtures compared to the non-doped samples. Additionally single-doped samples with Ca and Sr have lower densities than samples doped with Ba, which is also true for samples with two dopants. The measured numbers are listed in Table 6 in the Appendix.

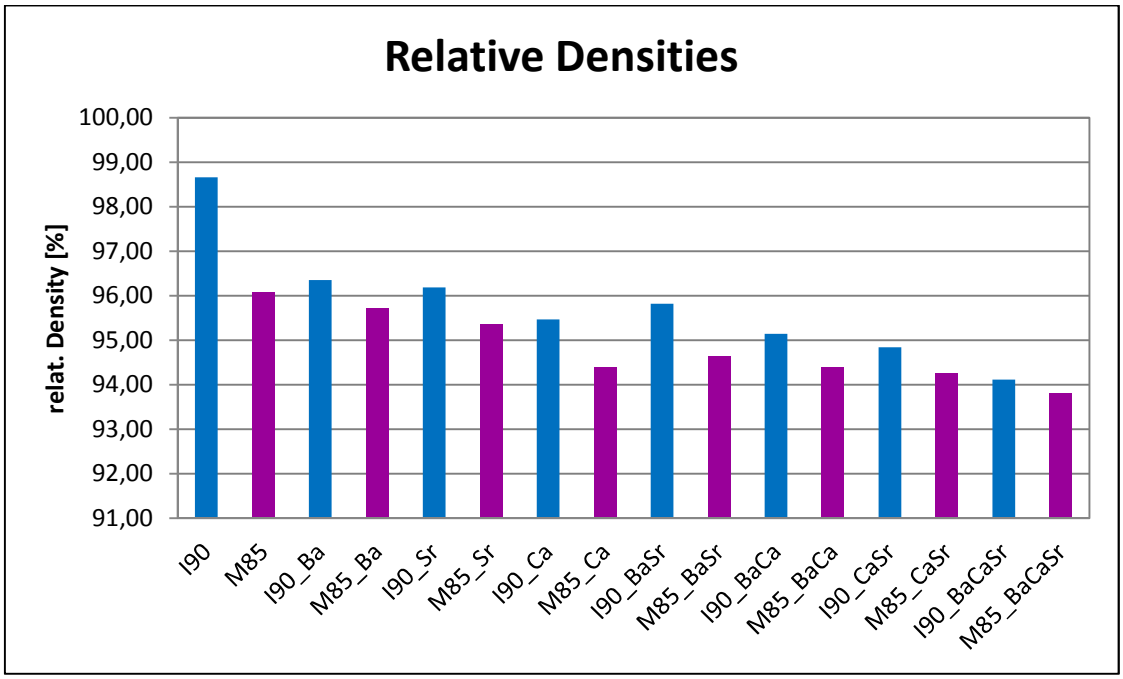

Figure 29: Relative densities of the samples after sintering

4.2.5 Shrinkage Studies

It was observed that during sintering all samples loose between 14 % and 18 % in diameter and between 12 % and 18 % in height. No significant influences of different dopant concentrations can be found.

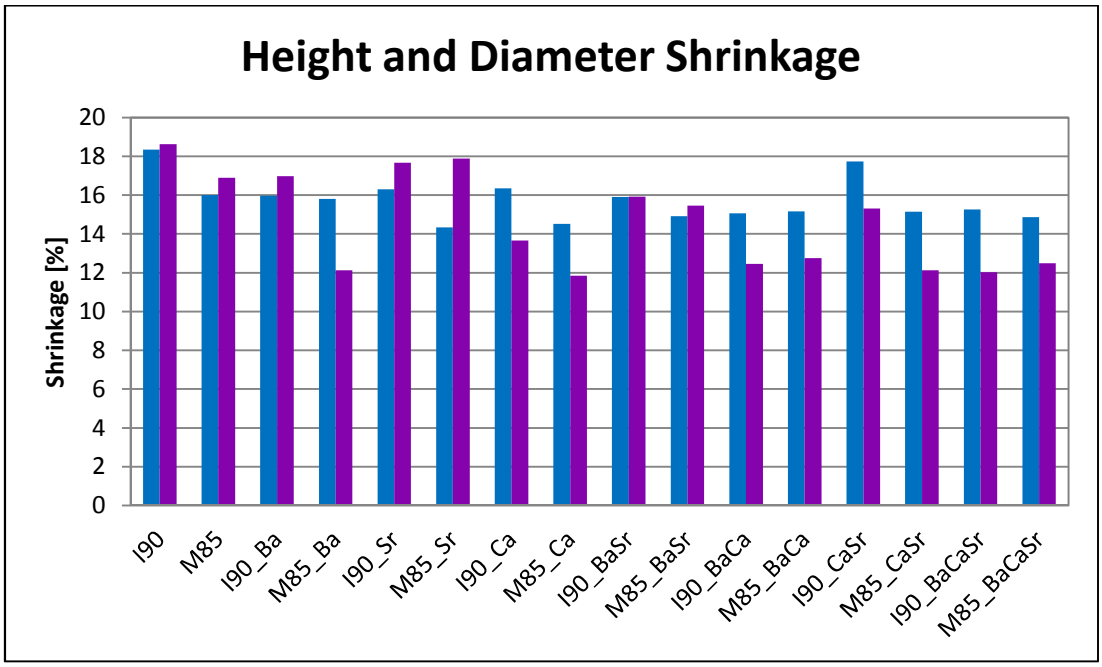

Figure 30: Shrinkage in height and diameter, where the blue bars are indicating the shrinkage in diameter and the violet bars indicating the shrinkage in height

4.2.6 Electron Microscopy Analysis

Figure 31 - Figure 34 show the SEM images of the non-doped and fully doped I90 and M85 compositions respectively. Pictures of the other mixtures can be found in the Appendix (see 6.2.1). As it can be seen in Figure 35, for the non-doped samples the PLZT (6/90/10) composition has larger grains than the PLZT (6/85/15) mixture while the grain sizes start to assimilate with the amount of dopants present. For all compositions it can be show that the addition of the alkaline earth metals increases the grain size, this is especially true for the compositions containing calcium (see Figure 35).

As already stated in the Materials and Methods section, the EDX analysis did not yield sufficient data to allow a calculation of the exact elemental composition within the phases detected. Therefore only an excerpt of the images taken will be shown in the Appendix (see 6.2.2). It can be stated that for all samples a secondary lead rich phase was detected. This might be due to the not reacted free lead which is forming a liquid phase between the grains during sintering.

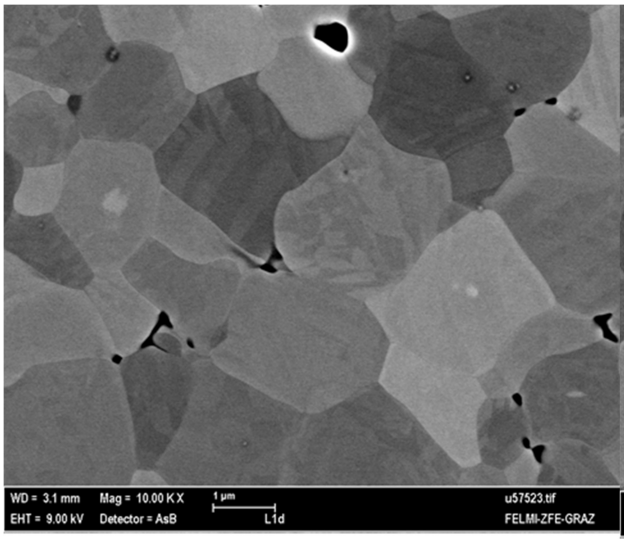

Figure 31: micrograph of non-doped I90

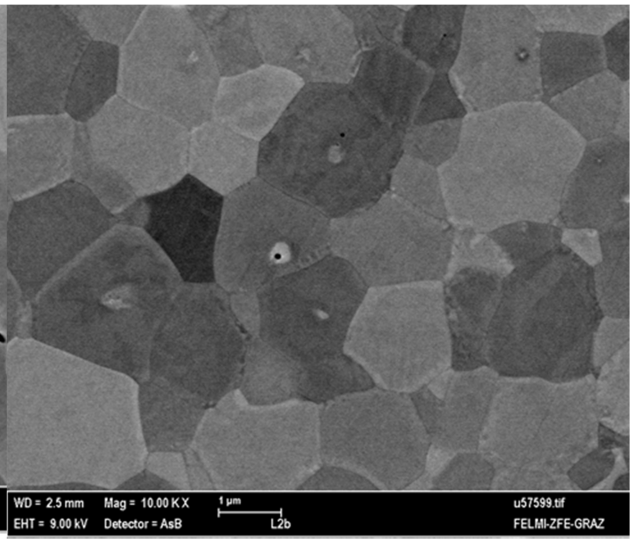

Figure 32: micrograph of non-doped M85

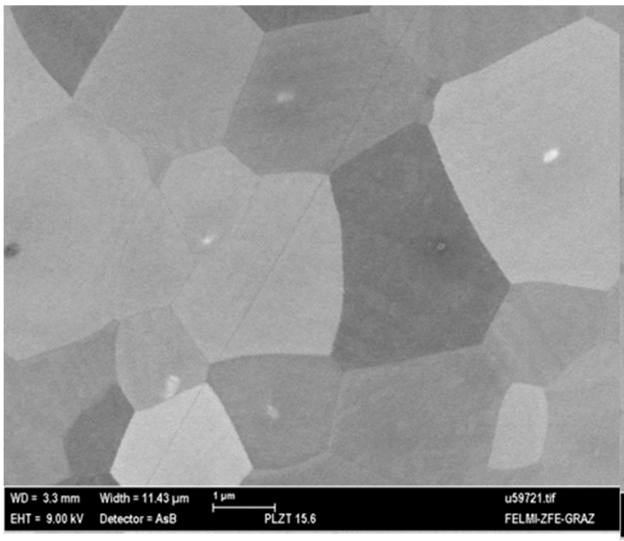

Figure 33: micrograph of full doped I90

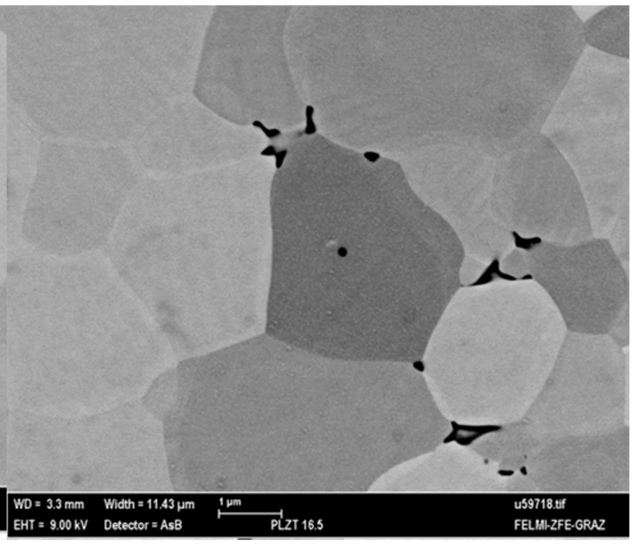

Figure 34: micrograph of full doped M85

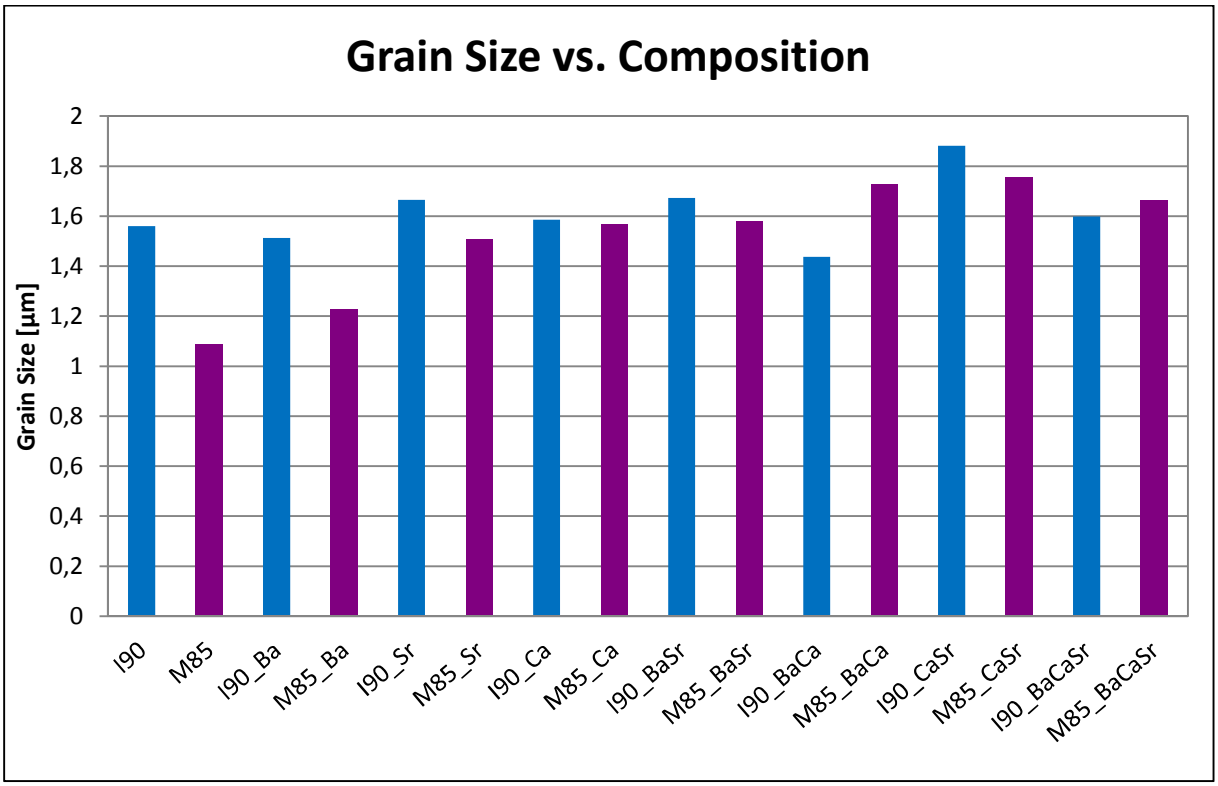

Figure 35: Comparison of grain sizes – yielded via the Line-Section-Method

4.3 Electric Characterization

The piezoelectric properties of the two main compositions will be discussed in one chapter, while the low and high signal measurements will be discussed separately to allow a better comparison among them. In the summary an overview about the differences between the samples will be given.

4.3.1 Piezoelectric Constant d_{33}

Figure 36 and Figure 37 show the average values for the piezoelectric constant taken out of 8 measurements for each composition with the I90 samples yielding higher values than the M85 samples. The obtained data show a very low piezoelectric constant; this proves the existence of an antiferroelectric material with a low remanent polarization.

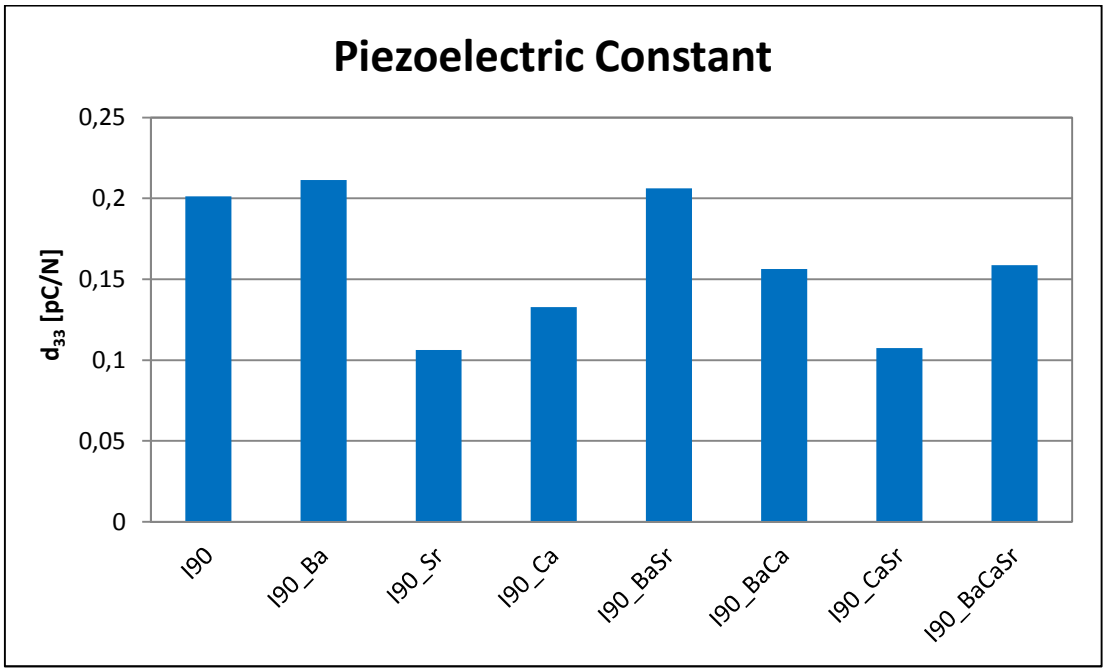

Figure 36: Piezoelectric constant of the samples based on the I90 mixture

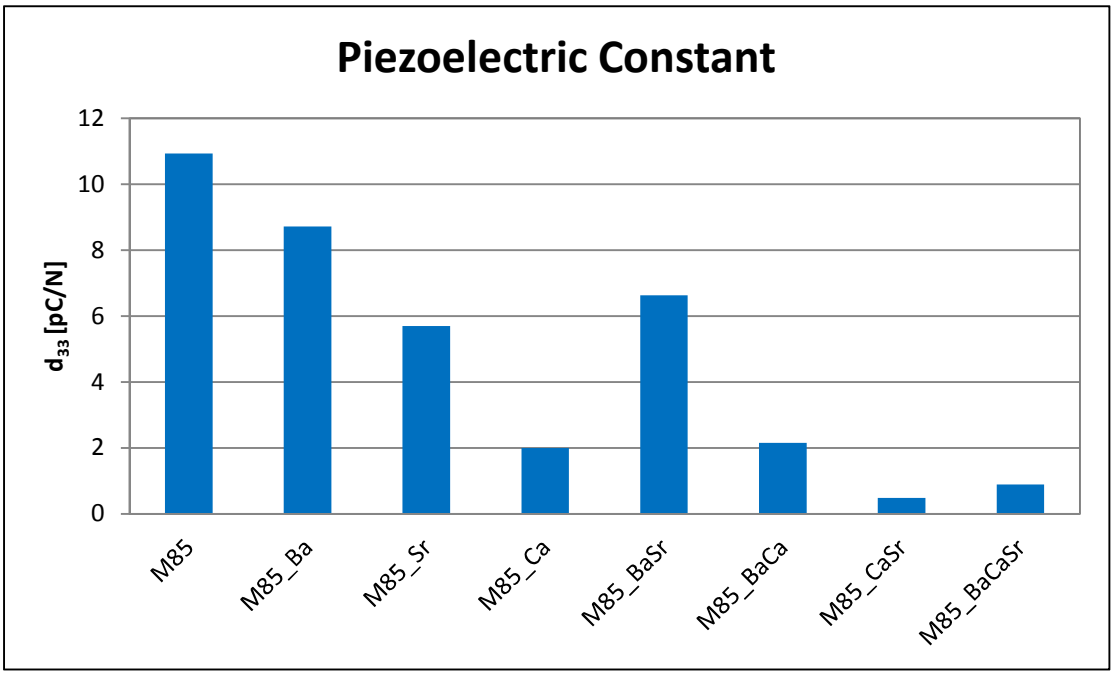

Figure 37: Piezoelectric constant of the samples based on the M85 mixture

4.3.2 I90: PLZT (6/90/10)

4.3.2.1 Low Signal Measurements

Figure 38 and Figure 39 show the measured values for the relative permittivity and the loss factor respectively. The measurements were carried out at 1 kHz and 10 kHz prior and after poling with 5 kV.

4.3.2.1.1 Relative permittivity

While the sample containing only strontium showed an increase in the relative permittivity after poling, the values for the mixture doped with only calcium remained stable. Except for these two single-doped samples all compositions showed a lower relative permittivity after the poling took place.

The addition of barium slightly increases the relative permittivity compared to the I90 basic mixture for about 10 % for the non-poled and up to 4 % for the poled samples. On the other hand strontium and calcium lower the permittivity for 15 % and up to 30 % for the non-poled composition containing strontium measured at 1 kHz. Again the addition of barium to strontium or calcium containing samples levels out the decreasing effect. For the I90_BaCa sample only a small decrease of 4 % for the non-poled and 6 % for the poled samples was measured. The fully doped samples also showed a small decrease in the permittivity of around 10 % compared to the non-doped sample.

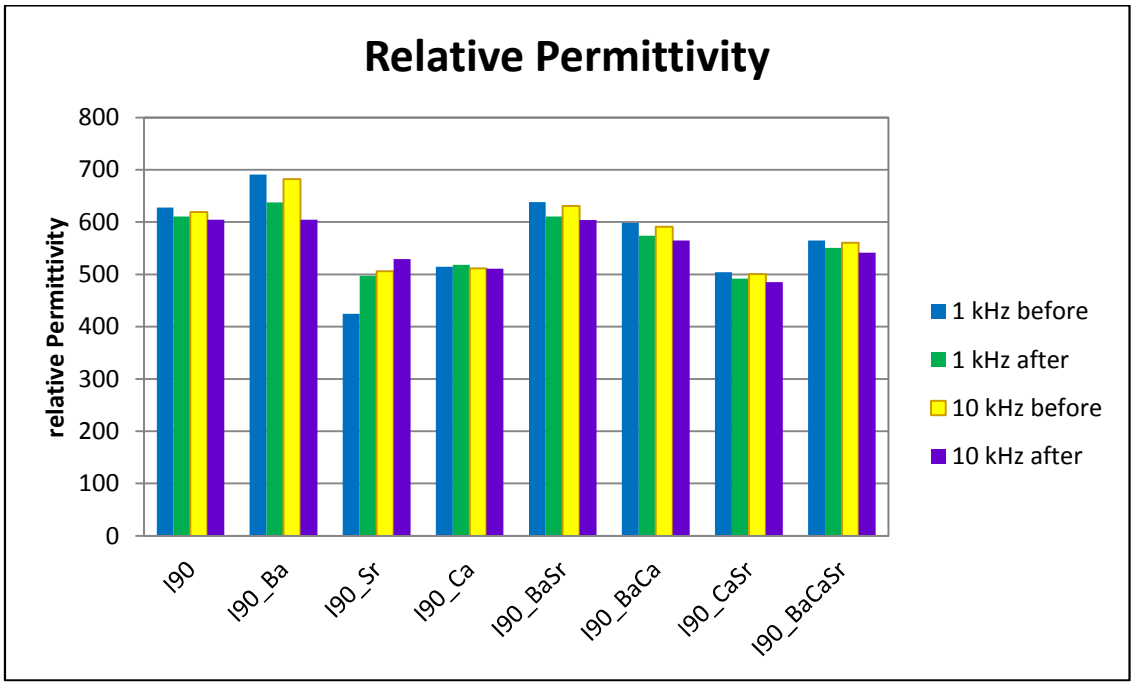

Figure 38: Relative permittivity (ε) of the samples based on the I90 mixture prior and after poling

4.3.2.1.2 Loss Factor

Here the addition of both, barium and strontium show a significant increase in the loss factor for non-poled and poled samples. The highest increase could be detected for the poled samples measured at 10 Hz, where the values rose to more than 100 % compared to those of the I90 composition. However, this effect was not found in the multi doped samples containing barium and strontium where a decrease of 2 % - 5 % was detected. Samples containing calcium also showed a decrease in the values compared to the non-doped samples. However, in all cases poling of the samples lead to a higher loss factor.

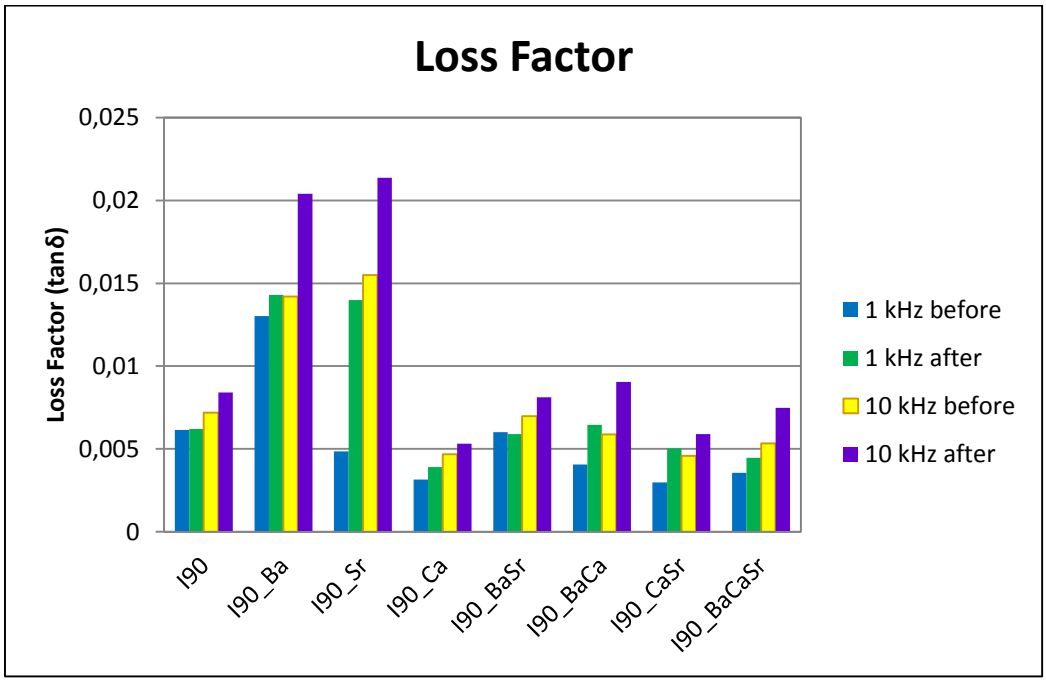

Figure 39: Loss factor (tanδ) of the samples based on the I90 mixture prior and after poling

4.3.2.2 High Signal Measurements

Figure 40 - Figure 45 show the obtained loops for the high signal measurements. Due to the fact, that the breakdown voltage of all samples of this compositions is below the switching field, no significant results could be obtained. However, it can be seen that the addition of barium causes a non-linear onset of the polarization curve (Figure 40), which gives evidence for a lower switching field. This is also true for the multi-doped samples (Figure 41). The same effect could also be seen in the current and strain measurements (see Figure 42 – Figure 45).

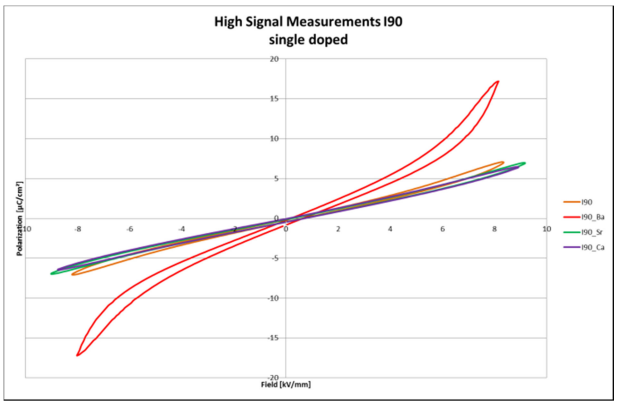

Figure 40: Hysteresis loops of single doped I90 compositions

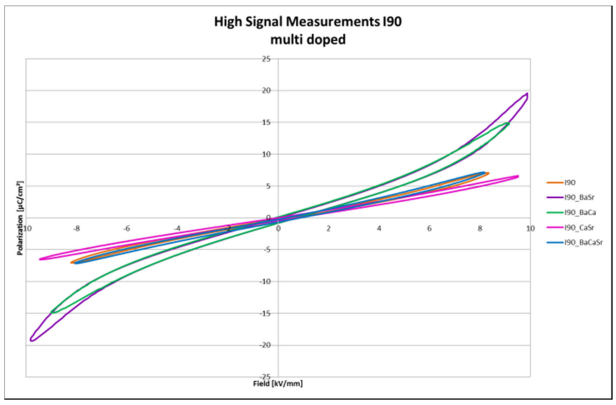

Figure 41: Hysteresis loops of multi doped I90 compositions

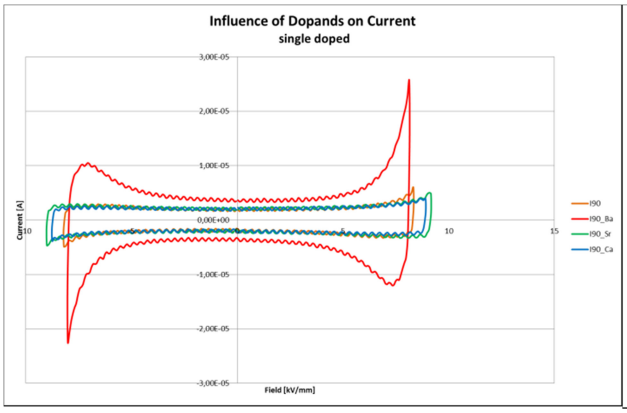

Figure 42: Field/Current-loops of single doped I90 compositions

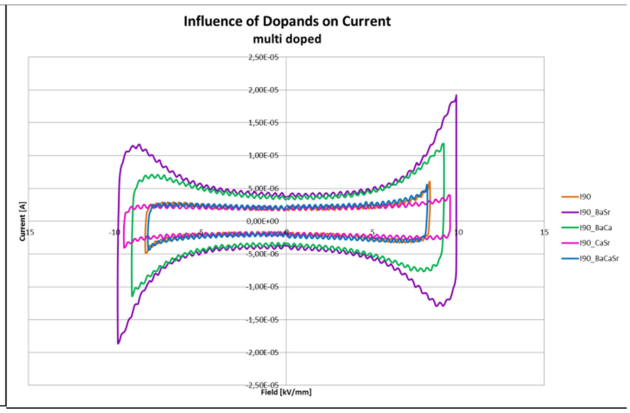

Figure 43: Field/Current-loops of multi doped I90 compositions

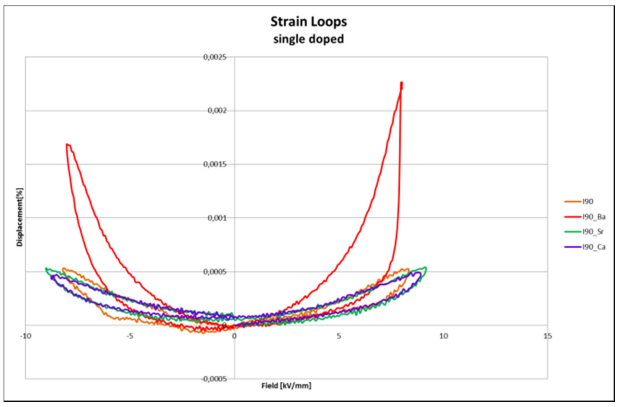

Figure 44: Strain-loops of single doped I90 compositions

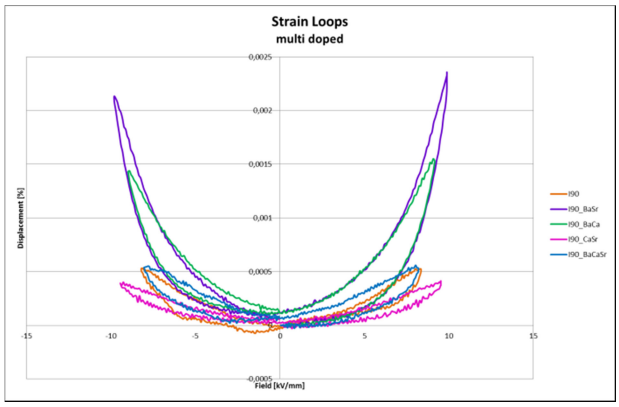

Figure 45: Strain-loops of multi doped I90 compositions

4.3.3 M85: PLZT (6/85/15)

In contrast to the I90 mixtures, the M85 samples did yield analyzable results for both, the low and the high signal measurements. To give an overview, the characteristic data for this composition can be found in the Appendix, see Table 7.

4.3.3.1 Low Signal Measurements

Figure 46 and Figure 47 show the measured values for the relative permittivity and the loss factor respectively. The measurements were carried out at 1 kHz and 10 kHz prior and after poling with 5 kV.

4.3.3.1.1 Relative permittivity

Except for the single-doped sample containing barium, the relative permittivity is increasing after the poling. The sample containing only strontium and the one doped with calcium and strontium showed the smallest increase.

For all compositions an increase in the relative permittivity of the non-poled samples could be measured. The highest increase within single doped samples was obtained for the mixture containing barium (up to 54 %) while strontium showed smaller effect (2 % - 20 % increase). The compositions containing barium and strontium, the one containing barium and calcium as well as the fully doped one showed the highest increases for both, non-poled and poled samples.

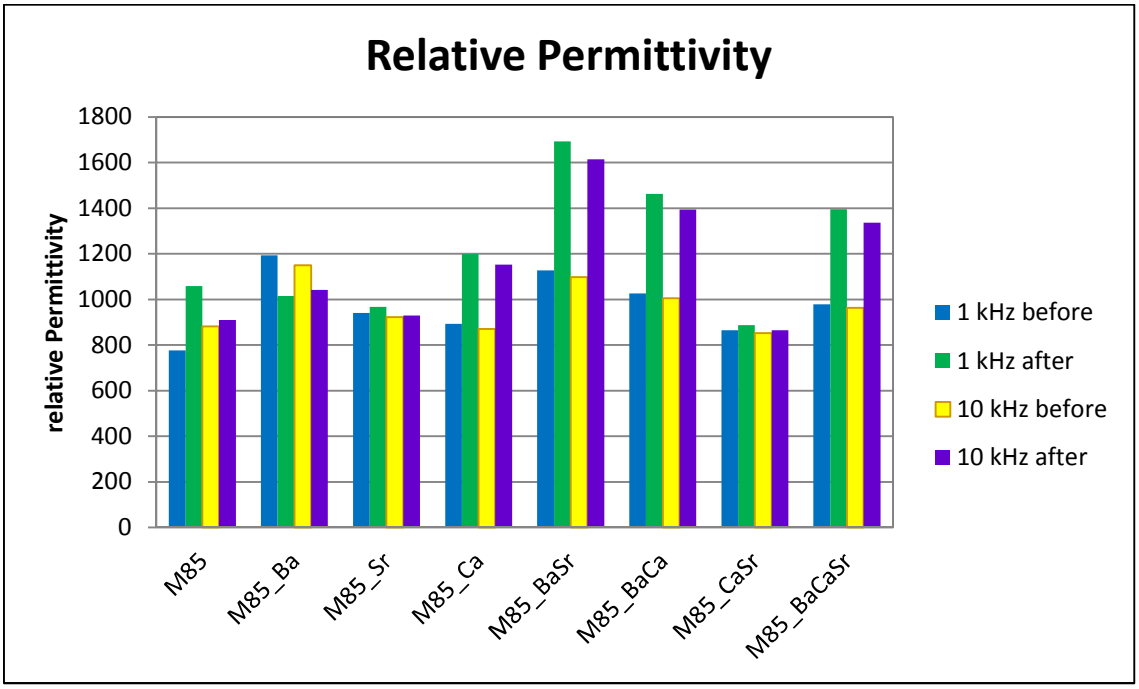

Figure 46: Relative permittivity (ε) of the samples based on the M85 mixture prior and after poling

4.3.3.1.2 Loss Factor

Here the addition calcium and strontium show a significant decrease in the loss factor for non-poled and poled samples. However, this effect was not found in the multi doped samples containing barium and strontium where a decrease of 2 % - 5 % was detected. Samples containing calcium also showed a decrease in the values compared to the non-doped samples. However, in all cases poling of the samples lead to a higher loss factor.

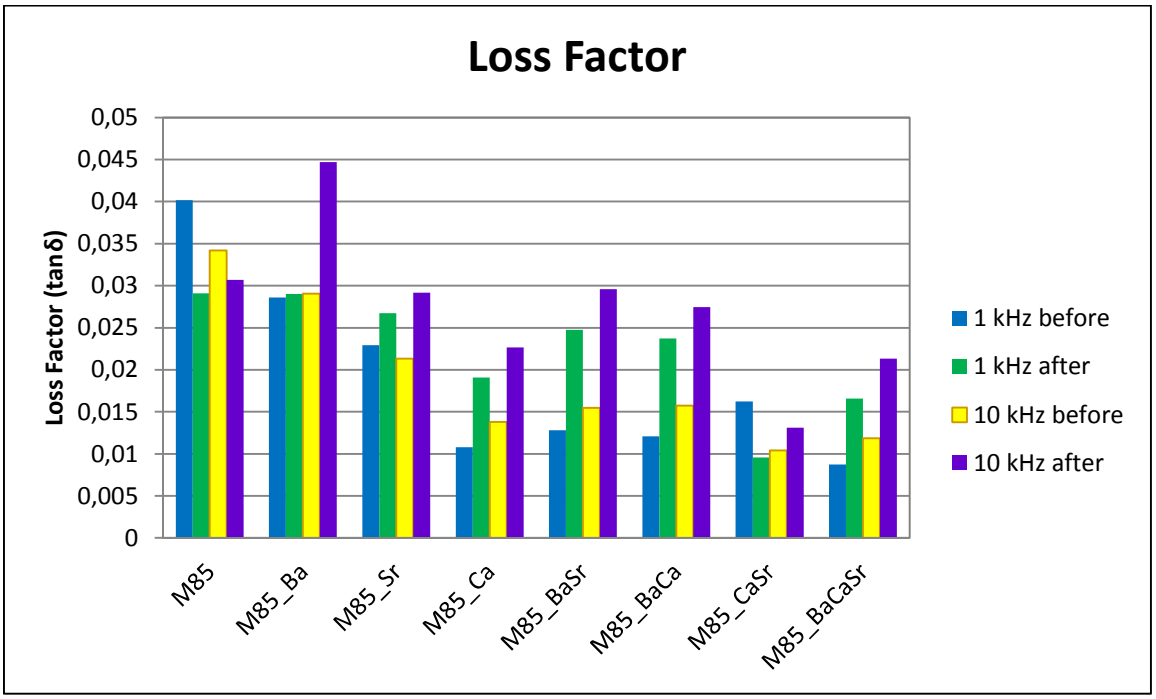

Figure 47: Loss factor (tanδ) of the samples based on the M85 mixture prior and after poling

4.3.3.2 High Signal Measurements

As it can be seen in Figure 48 and Figure 49 the addition of barium lowers the switching field for the single as well as for the multi-doped samples, while doping with strontium and calcium leads to an increase in the switching field. This results in the multi doped sample containing Ca and Sr having the highest switching field. The addition of barium to samples containing calcium and strontium does decrease the switching field. However for all multi doped samples containing calcium the breakdown voltage was lower than the field necessary to allow proper measuring.

Figure 50 and Figure 51 show field vs. current loops for the single and multi-doped mixtures respectively. The single-doped sample containing barium shows a shift of the current-peaks to lower values while strontium and calcium cause an increase in the measured values. As the non-doped sample, the M85_Ba shows an additional peak at 1 kV, which also can be found in the multi-doped sample containing barium and strontium. However this peak cannot be found in other compositions of this series.

The strain loops show a decrease in displacement for the sample containing barium; this is also true for the composition doped with calcium. The same effect was observed in the multi-doped samples.

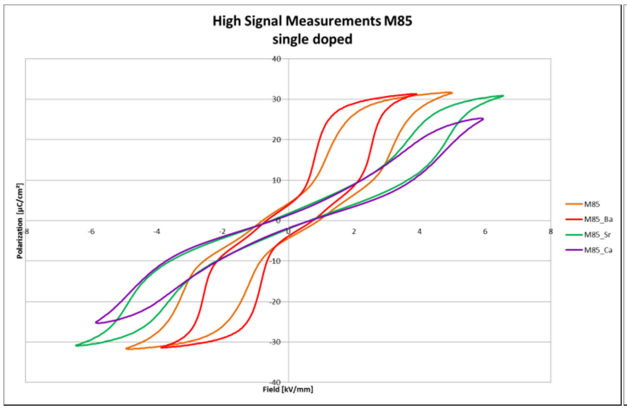

Figure 48: Hysteresis loops for single doped M85 compositions

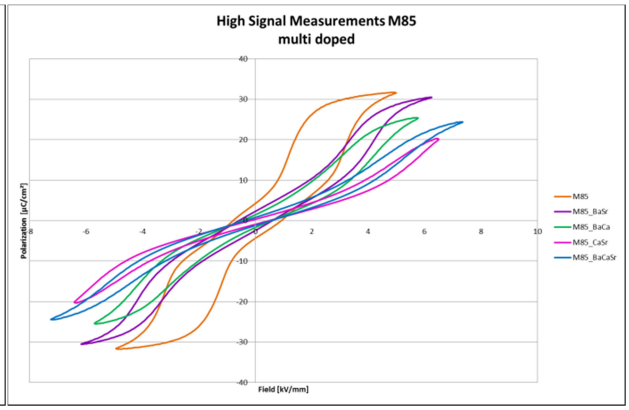

Figure 49: Hysteresis loops for multi doped M85 compositions

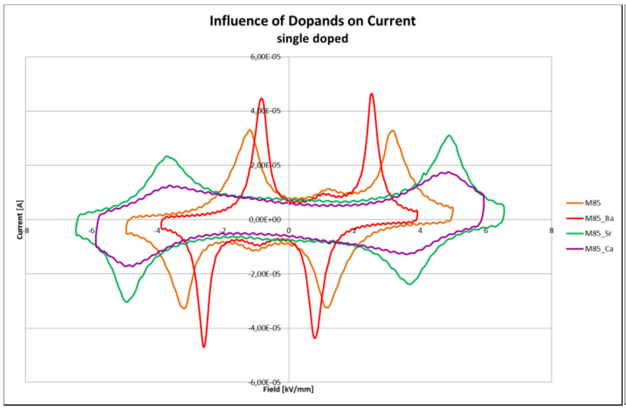

Figure 50: Field/Current-loops for the single doped M85 compositions

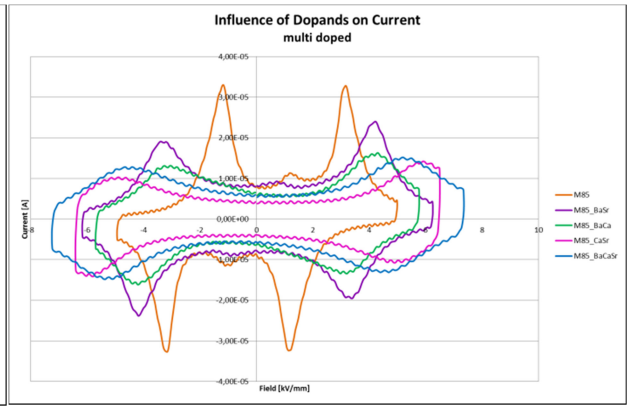

Figure 51: Field/Current-loops for the multi doped M85 compositions

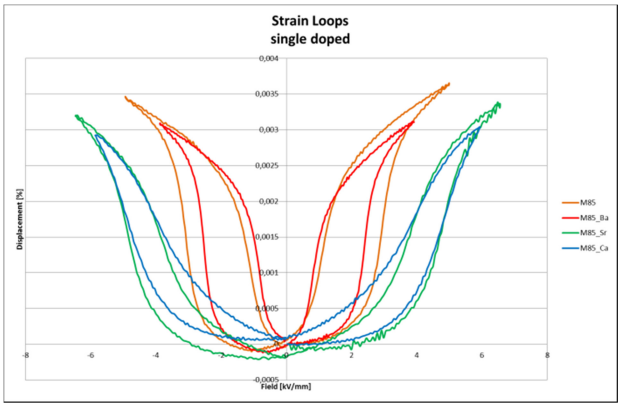

Figure 52: Strain loops for the single doped M85 compositions

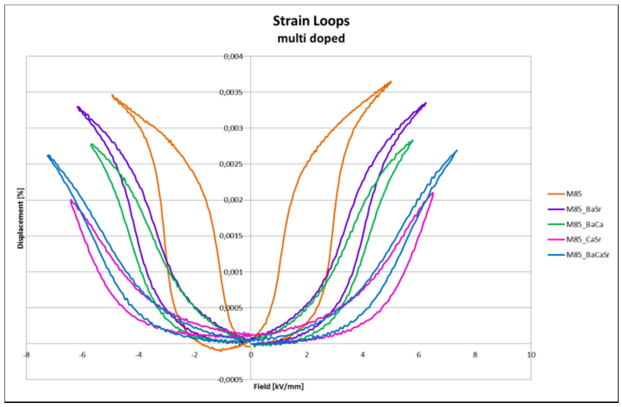

Figure 53: Strain loops for the multi doped M85 compositions

4.3.3.2.1 High Signal Energy Loss

Figure 54 shows the difference in the switching field for forward and backward polarization, ΔE, which is proportional to the energy loss during cycling. All dopants decrease the loss of energy. The composition containing calcium and strontium exhibits the lowest energy loss of all mixtures. For a complete analysis, please refer to Table 7 in the Appendix.

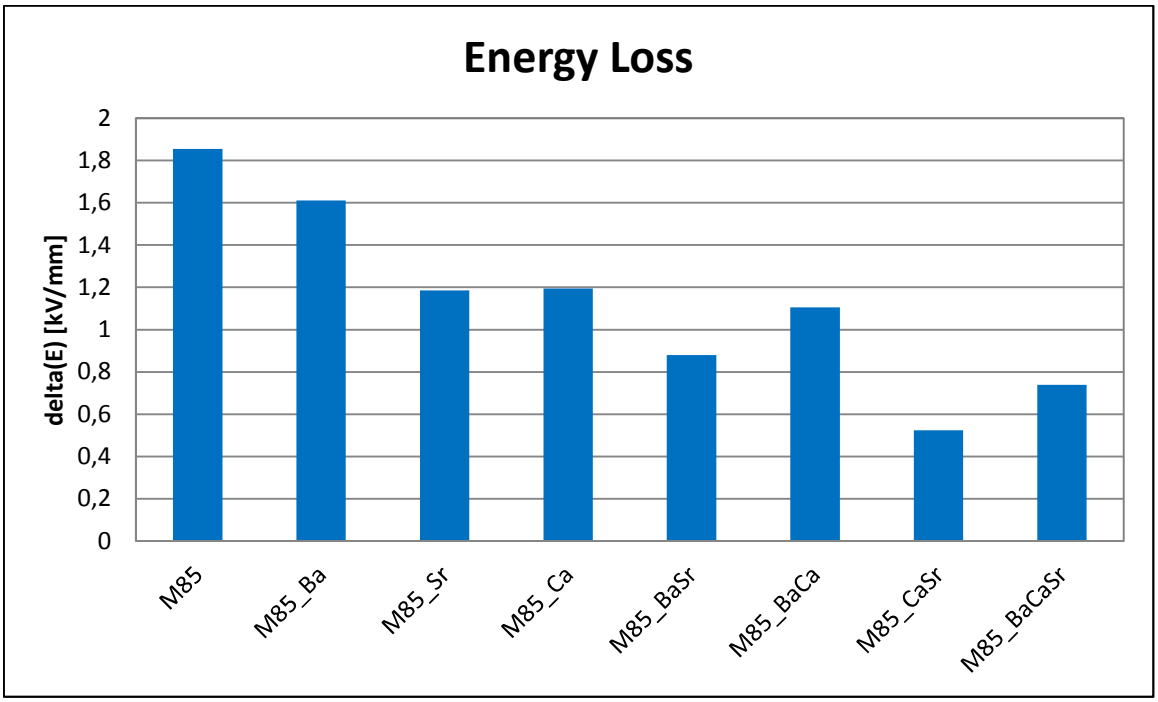

Figure 54: High signal energy loss

4.3.3.2.2 Switching Field vs. Tolerance Factor vs. Effective Mass (A-site)

To show the relationship between the ionic radius, which is expressed by the tolerance factor, the effective mass of A-site ions and the switching field a 3D-presentation was chosen and filled with data from the M85 series (Figure 19). It can be shown that with increasing effective mass the switching field decreases, this is also true for the Goldschmidt's tolerance factor.

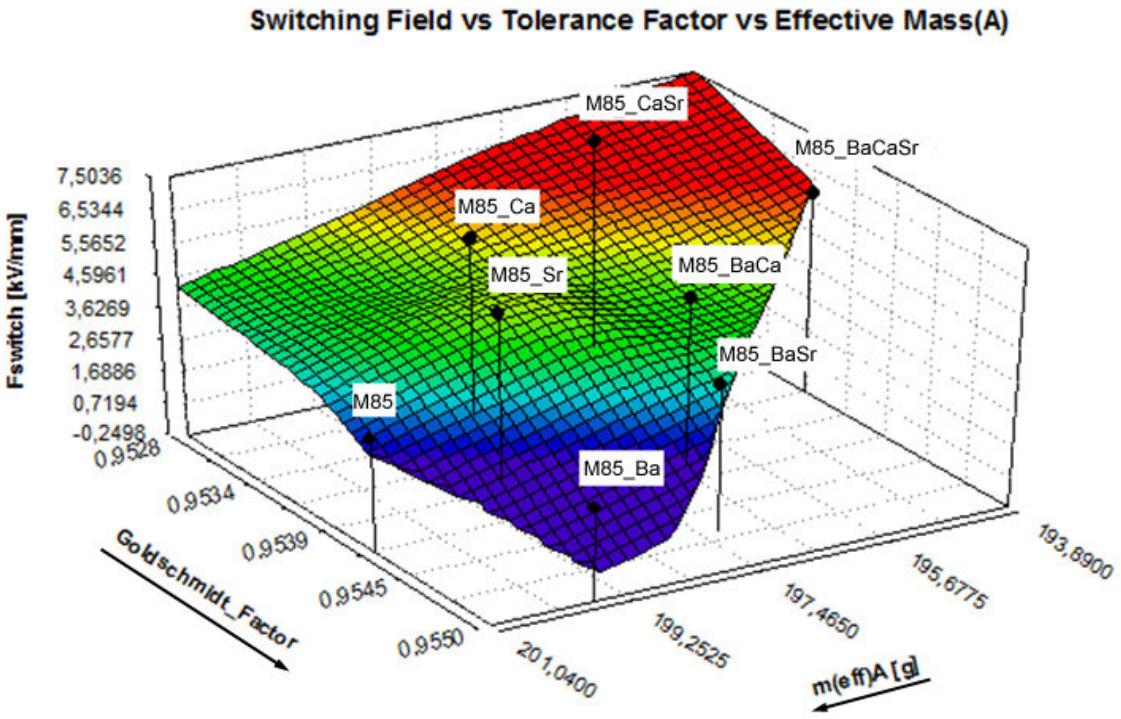

Figure 55: 3D-Diagram of switching field vs. Goldschmidt's tolerance factor vs. effective mass at A-site for the M85 composition

5 Summary

The major aim of this work is to study the influence of alkaline earth dopants, such as Ba, Ca and Sr on the antiferroelectric properties of lanthanum modified lead zirconate-titanate. Two basic compositions with differing Zr/Ti-ratio were mixed with varying concentrations of the alkaline earth dopants according to the following formula: $(Pb_{0,91-x-y-z}Ba_xCa_ySr_zLa_{0,06})(Zr_{1-m}Ti_m)O_3$ (x, y, z = 0 & 0,02, m = 0,10 & 0,15). This leads to 16 different compositions in total. The samples containing 90 % zirconium were labeled I90, while the mixtures with 85 % zirconium are designated M85.

The numbers calculated for Goldschmidt's tolerance factor and the effective mass at the A-site of the perovskite lattice plotted create a grid allowing it to make assumptions for further materials. It was found that the samples containing less titanium possessed a higher Goldschmidt factor.

The results obtained by Dilatometry show similar sintering behavior for the materials analyzed thus allowing the same sintering temperature for all compositions. It could have been proved that the sinter design is crucial for obtaining dense ceramic samples. The importance of maintaining the atmosphere during the sintering step by means of lead oxide containing sintering powder also was shown.

The weight loss studies during calcination showed a clear dependence on the dopant concentration whereas no clear influence of the Zr/Ti-ratio could be found. The non-doped samples had the lowest weight loss of about 1,5 % while the fully doped samples had losses up to 3 %. For the calculations of those numbers it was assumed that the measured weight loss was solely due to the dissociation of Pb_3O_4 and further vaporization of the lead.

The XRD analysis of the calcined and sintered samples gave evidence for the formation of the perovskite structure, however due to the refinement data no predication about secondary phases can be made. Comparing the volume of the unit cells again a clear influence of dopants can be seen. The changes in the volumes of the unit cell agree with the changes of average ionic radii which indicates the substitution of lead by the alkaline earth ions.

The density measurements show a strong influence of the dopants on the relative densities as well. While for the non-doped and single doped samples the I90 compositions always possess higher densities with increasing dopant concentrations the values are assimilating. Single doped samples with Ca and Sr have lower densities than samples doped with Ba. In the shrinkage studies no significant influences of dopants could be found.

In the electron microscopy analysis it was found that for the non-doped samples the I90 composition has larger grains than the M85 mixture while the grain sizes start to assimilate with the amount of dopants present. For all compositions it can be show that the addition of the alkaline earth metals increases the grain size, this is especially true for the compositions containing calcium. In all samples a secondary lead rich phase could be detected.

The measurement of the piezoelectric constant showed the existence of an antiferroelectric material with a low remanent polarization. The M85 mixtures yielded higher values than the I90 samples.

In case of the I90 mixtures, the relative permittivity decreased after poling, except for the single-doped samples containing strontium, where an increase could be detected. However, for the M85 compositions it was found that the single-doped sample containing barium was the only one that showed a decrease in the relative permittivity. All other samples of this series had an increased relative permittivity after the poling. In all cases the relative permittivity of the M85 samples was higher than the one of the I90 samples. While barium increases the permittivity, calcium and strontium lower its values. The fully doped I90 samples showed a small decrease in permittivity compared to the non-doped samples. The M85 compositions containing barium and strontium, barium and calcium as well as the fully doped samples showed the highest increases in permittivity.

The high signal measurements done for the I90 compositions did not adduce results, however it can be stated that the addition of barium causes a non-linear onset of the polarization curve, which gives evidence for a lower switching field.

In case of the M85 samples, the addition of barium lowers the switching field for the single as well as for the multi-doped samples. Doping with strontium and calcium leads to an increase in the switching field.

The field vs. current loops for the single-doped sample containing barium shows a shift of the current-peaks to lower values while strontium and calcium cause an increase in the measured values. As the non-doped sample, the M85_Ba shows an additional peak at 1 kV, which also can be found in the multi-doped sample containing barium and strontium. However this peak cannot be found in other compositions.

The strain loops show a decrease in displacement for the sample containing barium; this is also true for the composition doped with calcium. The same effect was observed in the multi-doped samples.

Analyzing the energy loss during hysteresis for the M85 compositions showed that all dopants decrease the loss of energy. The composition containing calcium and strontium exhibits the lowest energy loss of all mixtures.

Summarizing it can be said that the amount and type of dopants in PLZT do have an effect not only on the electrical properties but also during the sintering my means of grain growth. Differences in the behavior could be detected not only within the two basic compositions but also between them. As in general when sintering lead containing ceramics the set-up and the atmosphere during sintering are crucial for preventing a high loss of lead and ensuring dense ceramic bodies.

6 Appendix

6.1 X-Ray Diffraction Analysis

Table 5: Calculated values from XRD Analysis

Calcination	**Unit Cell**				**Theoretic Density**	
	Lattice Parameter			**Volume**	**By Software**	**Calculated**
Sample	a [Å]	b [Å]	c [Å]	V [Å³]	ρ_{theo} [g/cm³]	ρ_{theo} [g/cm³]
I90	5,83	5,83	14,35	422,94	7,96	7,82
M85	5,83	5,83	14,37	422,56	7,96	7,77
I90_Ba	5,83	5,83	14,35	422,97	7,95	7,78
M85_Ba	5,83	5,83	14,36	423,36	7,95	7,72
I90_Sr	5,83	5,83	14,35	422,60	7,95	7,77
M85_Sr	5,83	5,83	14,36	423,32	7,95	7,70
I90_Ca	5,83	5,83	14,34	422,00	7,97	7,74
M85_Ca	5,83	5,83	14,36	423,07	7,95	7,67
I90_BaSr	5,83	5,83	14,35	422,53	7,96	7,74
M85_BaSr	5,83	5,83	14,36	423,14	7,95	7,68
I90_BaCa	5,83	5,83	14,34	422,19	7,97	7,72
M85_BaCa	5,83	5,83	14,35	422,66	7,96	7,66
I90_CaSr	5,82	5,82	14,34	421,22	7,99	7,71
M85_CaSr	5,83	5,83	14,35	422,62	7,96	7,64
I90_BaCaSr	5,83	5,83	14,34	422,16	7,97	7,66
M85_BaCaSr	5,83	5,83	14,35	422,31	7,97	7,61
Sintering	**Unit Cell**				**Theoretic Density**	
	Lattice Parameter			**Volume**	**By Software**	**Calculated**
Sample	a [Å]	b [Å]	c [Å]	V [Å³]	ρ_{theo} [g/cm³]	ρ_{theo} [g/cm³]
I90	5,83	5,83	14,32	421,56	7,98	7,84
M85	5,82	5,82	14,29	419,32	8,02	7,83
I90_Ba	5,83	5,83	14,32	421,88	7,98	7,80
M85_Ba	5,82	5,82	14,29	419,64	8,02	7,79
I90_Sr	5,83	5,83	14,31	421,21	7,99	7,79
M85_Sr	5,82	5,82	14,29	419,14	8,03	7,78
I90_Ca	5,82	5,82	14,30	419,97	8,01	7,78
M85_Ca	5,81	5,81	14,27	417,43	8,06	7,78
I90_BaSr	5,83	5,83	14,31	421,32	7,99	7,77
M85_BaSr	5,82	5,82	14,29	419,26	8,03	7,75
I90_BaCa	5,82	5,82	14,30	420,08	8,01	7,76
M85_BaCa	5,81	5,81	14,28	418,03	8,05	7,74
I90_CaSr	5,82	5,82	14,29	419,37	8,02	7,75

M85_CaSr	5,81	5,81	14,27	417,41	8,06	7,73
I90_BaCaSr	5,81	5,81	14,27	417,78	8,05	7,74
M85_BaCaSr	5,81	5,81	14,27	417,81	8,05	7,69

6.1.1 Densities of the Sintered Samples

Table 6: Density Values

Sample	Apparent Density [g/cm³]	Theoretic Density [g/cm³]	Relative Density [%]
I90	7,873	7,98	98,66
M85	7,706	8,02	96,08
I90_Ba	7,689	7,98	96,35
M85_Ba	7,677	8,02	95,72
I90_Sr	7,685	7,99	96,18
M85_Sr	7,657	8,03	95,35
I90_Ca	7,647	8,01	95,47
M85_Ca	7,608	8,06	94,39
I90_BaSr	7,656	7,99	95,82
M85_BaSr	7,600	8,03	94,65
I90_BaCa	7,621	8,01	95,14
M85_BaCa	7,599	8,05	94,40
I90_CaSr	7,606	8,02	94,84
M85_CaSr	7,598	8,06	94,27
I90_BaCaSr	7,576	8,05	94,11
M85_BaCaSr	7,551	8,05	93,80

6.2 Electron Microscopy Analysis

6.2.1 SEM-Images

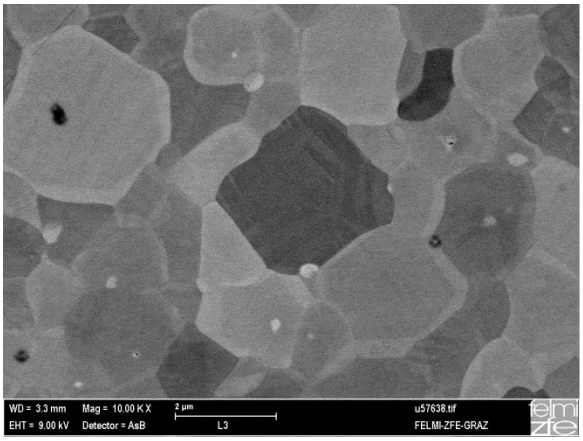

Figure 56: micrograph of I90_Ba

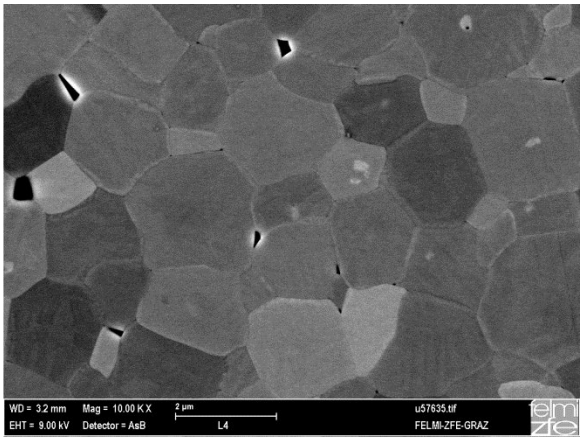

Figure 57: micrograph of M85_Ba

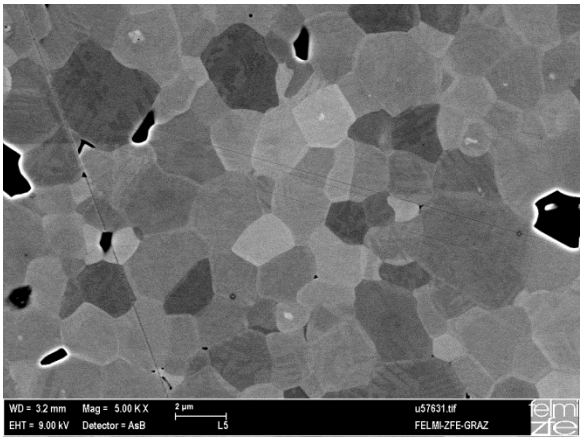

Figure 58: micrograph of I90_Sr

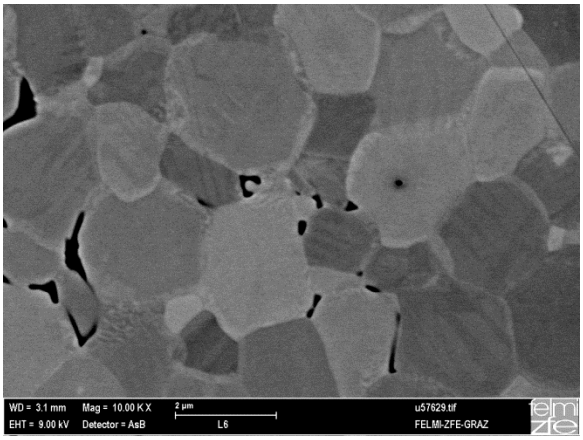

Figure 59: micrograph of M85_Sr

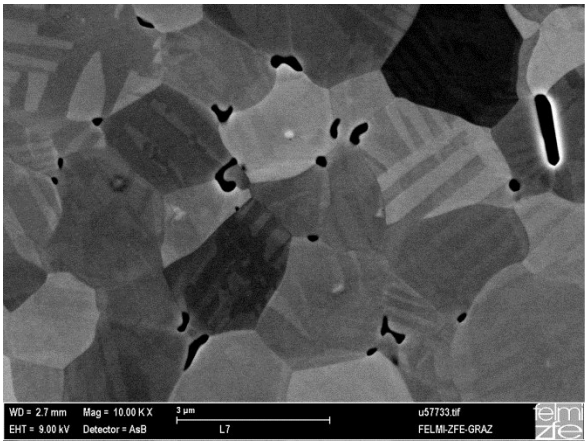

Figure 60: micrograph of I90_BaSr

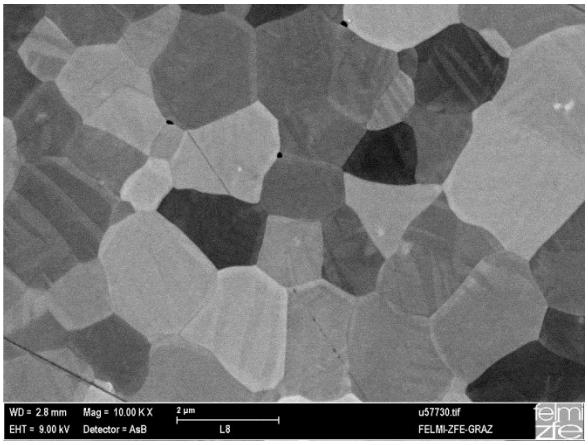

Figure 61: micrograph of M85_BaSr

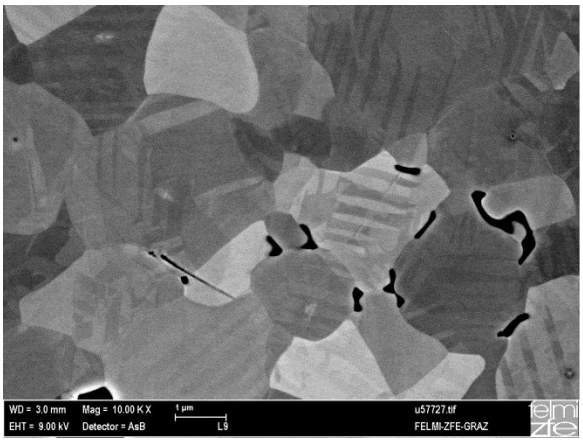

Figure 62: micrograph of I90_Ca

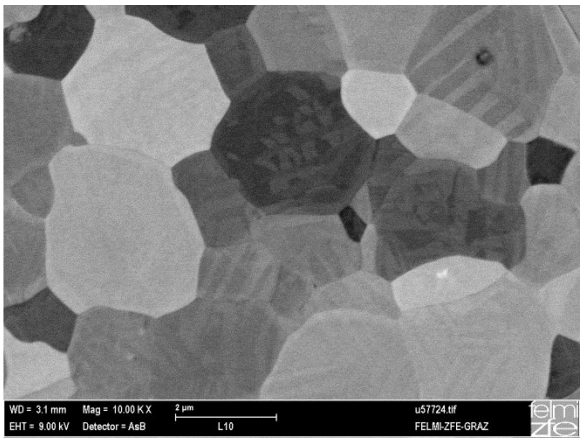

Figure 63: micrograph of M85_Ca

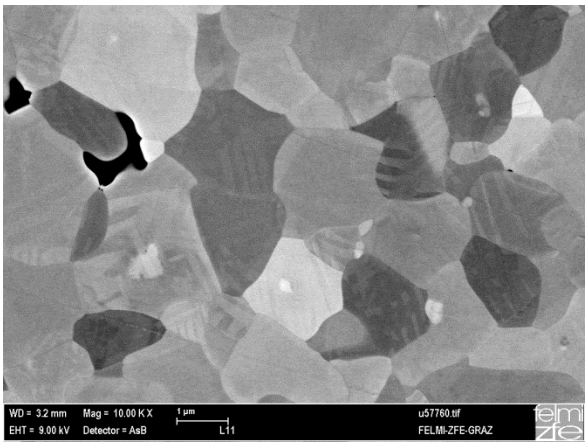

Figure 64: micrograph of I90_BaCa

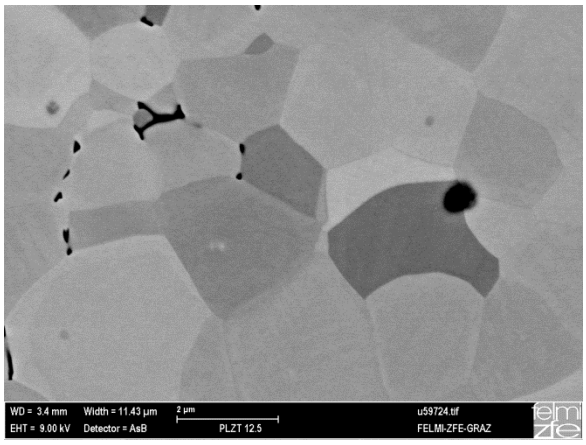

Figure 65: micrograph of M85_BaCa

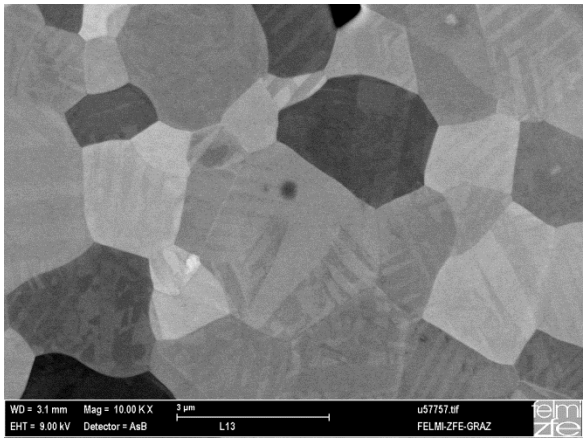

Figure 66: micrograph of I90_CaSr

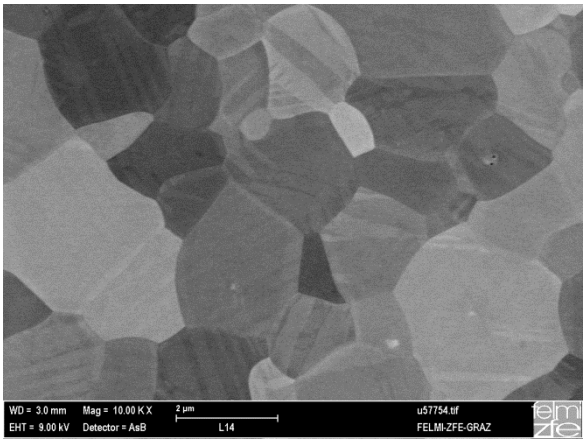

Figure 67: micrograph of M85_CaSR

6.2.2 Images for EDX Analysis

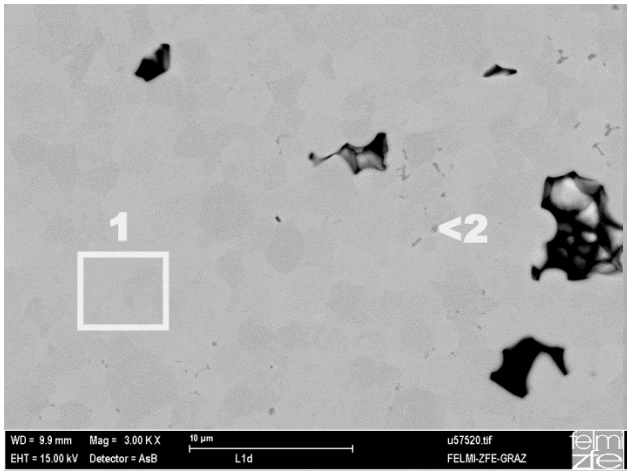

Figure 68: image of the phase distribution in a I90 sample, on can see the matrix (1), darker secondary lead rich phases (2) and pores

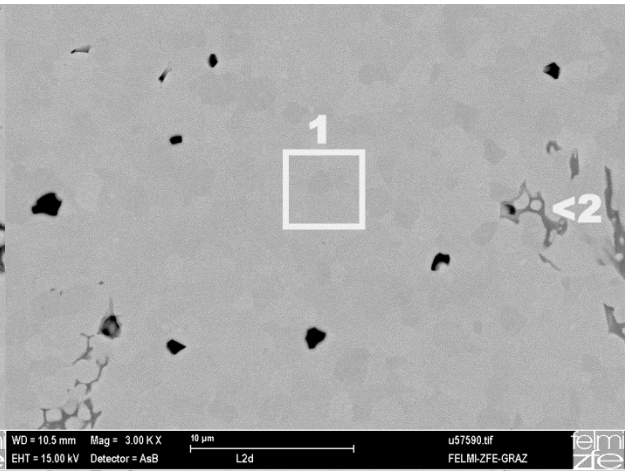

Figure 69: image of a M85 sample showing the phase distribution, again a secondary phase (2) with a higher lead concentration than the matrix (1) can be seen

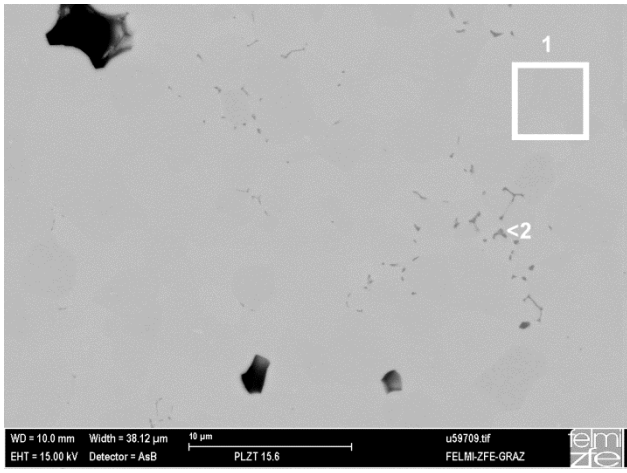

Figure 70: I90_BaCaSr sample showing a secondary lead rich phase (2), (1) indicates the matrix

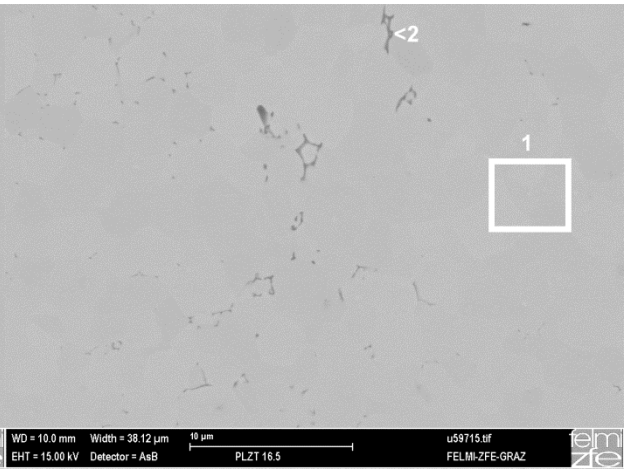

Figure 71: image of the M85_BaCaSr sample, again a lead rich phase (2) can be detected

6.3 M85: PLZT (6/85/15)

6.3.1 Electric Characterization

Table 7: Characteristics of M85 compositions

Sample	Goldschmidt Factor	Effective Mass(A)	d_{33} High Signal	max. Current	max. Polarization	max. Elongation	max. Field	Rem. Polarisation	Coercive Field	Polarization at Switching Field	Switching Field	Energy Loss
Composition		[g]	[nm/V]	[A]	[µC/cm²]	[%]	[kV/mm]	[µC/cm²]	[kV/mm]	[µC/cm²]	[kV/mm]	[kV/mm]
M85	0,954	201,030	0,735	3,30E-05	31,694	3,65E-03	4,992	4,410	-7,65E-01	18,10	3,275	1,854
M85_Ba	0,955	199,633	0,819	4,64E-05	31,346	3,12E-03	3,912	3,990	-6,40E-01	19,60	2,607	1,611
M85_Sr	0,954	198,639	0,653	3,10E-05	30,876	3,39E-03	6,553	1,900	-4,82E-01	20,80	4,957	1,186
M85_BaSr	0,955	197,241	0,657	2,56E-05	31,272	4,56E-03	6,735	2,520	-5,62E-01	20,00	4,292	0,88
M85_Ca	0,953	197,688	0,672	1,91E-05	27,296	8,58E-03	6,428	1,770	-5,36E-01	19,60	4,79	1,195
M85_BaCa	0,954	196,290	0,582	1,77E-05	26,382	4,47E-03	6,254	1,680	-5,22E-01	18,50	4,37	1,105
M85_CaSR	0,953	195,296	0,312	1,42E-05	20,266	2,10E-03	6,500	0,427	-1,55E-01	17,30	6,035	0,524
M85_BaCaSr	0,954	193,899	0,396	1,52E-05	24,414	2,69E-03	7,354	0,924	-3,21E-01	18,30	5,788	0,739

7 References

[1] A. J. Moulson und J. M. Herbert, Electroceramics: Materials, Properties, Applications. 2nd Edition, West Sussex, England: John Wiley & Sons Ltd., 2003.

[2] Y. Shimakawa, „A-Site-Ordered Perovskites with Intriguing Physical Properties," *Inorganic Chemistry,* Bd. Vol. 47, Nr. No. 19, p. 8562, 2008.

[3] K. w. Gachigi, *Eelctrical Energy Storage in Antiferroelectri-Ferroelectric Phase Switching. Chemically Modified Lead Zirconate Ceramics,* The Pennsylvania State University: Doctoral Thesis, 1997.

[4] C. Kittel, Einführung in die Festkörperphysik, 14. überarbeitete und erweiterte Auflage, München: Oldenbourg Wissenschaftsverlag GmbH, 2006.

[5] C. Weißmantel und C. Hamann, Grundlagen der Festkörperphysik, 4., bearbeitete Auflage, Heidelberg, Leipzig: Johann Ambrosius Barth Verlag, 1995.

[6] Y. Wang und C. Hoffmann, „Keramischer Werkstoff auf der Basis von der Perowskitkeramik BIO, 5NA0, 5Ti03, Piezoelektrischer Aktor enthaltend den keramischen Werkstoff und Verfahren zur Herstellung des keramischen Werkstoffs". Patent EP 2616411 A1, 24 Juli 2013.

[7] S. Hunklinger, Festkörperphysik, 2. Auflage, München: Oldenbourg Wissenschaftsverlag GmbH, 2009.

[8] J. Ravez, „Ferroelectricity in solid state chemistry," *C. R. Acad. Sci. Paris, Série IIc, Chimie/Chemistry 3,* pp. 267-283, 2000.

[9] H. Liu und B. Dhkil, „A brief review on the model antiferroelectric PbZrO3 perovskite-like material," *Z. Kristallogr. 226,* pp. 163-170, 2011.

[10] R. A. Mackie, A. Peláiz-Bararranco und D. J. Keelbe, „Vacancy defects in PbTiO3 and lanthanide-ion-doped PbTiO3: A study of positron lifetimes," *Physical Review B,* Nr. 82, pp. 024113-1, 2010.

[11] E. Breval, M. Klimkiewicz, C. Wang und J. P. Doherty, „Sinterabilitiy and Decomposition of Pb0,9175La0,055Zr0,975Ti0,025O3: Influence of Calcination and Sintering Temperature," *J. Am. Ceram. Soc.,* Bd. 90, Nr. 7, pp. 2043-2049, 2007.

[12] H.-B. Park, C. Y. Park, Y.-S. Hong, K. Kim und S.-J. Kim, „Structural and Dielectric Properties of PLZT Ceramics Modified with Lanthanide Ions," *J. Am.*

Ceram. Soc., Bd. 1, Nr. 82, pp. 94-102, 1999.

[13] D. Hennings und K. H. Härdtl, „The Distribution of Vacancies in Lanthana-Doped Lead Titanate," *Phys. Stat. Sol. (a),* Bd. 3, pp. 465-474, 1970.

[14] K. Ramam und K. Chandramouli, „Investigation on dielectric and piezoelectric characterization of PLSZT-BT ceramics," *Eur. Phys. J. Appl. Phys.,* Nr. 42, pp. 305-310, 2008.

[15] M. N. Rahaman, Ceramic Processing, Boca Raton, FL: CRC Press, Taylor & Francis Group, LCC, 2007.

[16] G. S. Snow, „Improvements in Atmosphere Sintering of Transparent PLZT Ceramics," *Journal of The American Ceramic Society,* Bd. 56, Nr. 9, pp. 479-480, 1973.

[17] B.-M. Song und D.-Y. Kim, „Effect of Excess PbO on the Densification of PLZT Ceramics," *J. Am. Ceram. Soc.,* Bd. 72, Nr. 5, pp. 833-836, 1989.

[18] D. A. Northrop, „Vaporization of Lead Zirconate-Lead Titanate Materials," *J. Am. Cer. Soc.,* Bd. 50, Nr. 9, pp. 441-445, 1967.

[19] S.-J. L. Kang, Sintering: Densification, Grain Growth & Microstructure, Oxford: Elsevier Butterworth-Heinemann, 2005.

[20] F. A. Kröger, The Chemistry of Imperfect Crystals, Amsterdam: North-Holland Publishing Company, 1964.

[21] A. Reichmann, A. Zankel, H. Reingruber, P. Pölt und K. Reichmann, „Direct observation of ferroelectric domain formation by environmental scanning electron microscopy," *Journal of the European Ceramic Society,* Bd. 31, Nr. 15, pp. 2939-2942, 2011.

[22] K. Ramam und V. Miguel, „Microstructure, dieelctric and ferroelectric characterization of Ba doped PLZT ceramics," *The European Physical Journal - Apllied Physics,* Bd. 35, pp. 43-47, 2006.

[23] Y. Shimakawa, „A-Site-Ordered Perovskites with Intriguing Physical Properties," *Inorganic Chemistry, Vol.47, No.19,* p. 8562, 2008.

8 List of Figures

FIGURE 1: SCHEMATIC OF A POLARIZED MATERIAL [1] 4

FIGURE 2: SCHEMATIC OF A DOMAIN STRUCTURE [5], A) MINIMIZING THE SIZE OF THE OUTER FIELD AND HENCE THE ENERGY BY FORMING MULTI-DOMAINS, B) IDEAL ARRANGEMENT OF 90° DOMAINS 5

FIGURE 3: ILLUSTRATION OF A DOMAIN STRUCTURE CHANGING ACCORDING TO OUTER INFLUENCES [1]; A) INITIAL STATE, NON-POLAR GRAINS; B) APPLIED ELECTRIC FIELD, NET-POLARITY IS FORMED; C) ELONGATION AND SWITCHING OF DOMAINS UNDER INCREASING APPLIED FIELD; D) DISORIENTATION OF DOMAINS DUE TO APPLIED STRESS 6

FIGURE 4: HYSTERESIS LOOPS OF A) LINEAR DIELECTRIC, AND NON-LINEAR DIELECTRICS B) FERROELECTRIC AND C) ANTIFERROELECTRIC MATERIAL, WITH CORRESPONDING PERMITTIVITY ε_{DERIV} VS ELECTRIC FIELD E [3] 7

FIGURE 5: POLARIZATION MECHANISMS [4] 10

FIGURE 6: PHASE DIAGRAM OF THE PZT SYSTEM [1] (SEE REF. [1] THEREIN) 12

FIGURE 7: BASIC FLOWCHART FOR THE PRODUCTION OF A CERAMIC BODY 14

FIGURE 8: SCHEMATIC ILLUSTRATION OF A SOLID-STATE REACTION [15] 16

FIGURE 9: IDEALIZED TWO-SPHERE MODEL, SHOWING DIFFERENCES IN SOLID-STATE AND LIQUID-PHASE SINTERING [15] 18

FIGURE 10: PORE STABILITY DEPENDING ON THE PORE COORDINATION NUMBER [15] 19

FIGURE 11: SINTERING STEPS [15] 20

FIGURE 12: APPARATUS FOR SINTERING PLZT [16] 21

FIGURE 13: PLZT SINTERING ARRANGEMENT 21

FIGURE 14: STEPS IN SAMPLE PREPARATION 25

FIGURE 15: TEMPERATURE PROGRAM FOR CALCINATION, THE DASHED LINE INDICATES THE NATURAL COOLING RATE, 5 HOURS HOLDING TIME AT 925°C 27

FIGURE 16: SINTERING ARRANGEMENT 28

FIGURE 17: TEMPERATURE PROGRAM FOR THE DEBINDERING STEP, THE DASHED LINE INDICATES THE NATURAL COOLING RATE, 1 HOUR HOLDING TIME AT 500 °C 29

FIGURE 18: TEMPERATURE PROGRAM FOR SINTERING, THE DASHED LINE INDICATES THE NATURAL COOLING RATE, 5 HOURS HOLDING TIME AT 1250 °C 29

FIGURE 19: EFFECTIVE MASS VS. TOLERANCE FACTOR, THE BLUE DOTS INDICATING MIXTURES OF THE I90 (PLZT (6/90/10)), THE RED DOTS INDICATING THE M85 (PLZT (6/85/15)) COMPOSITIONS 34

FIGURE 20: DILATOMETRIC ANALYSIS OF THE SINGLE AND FULLY DOPED SAMPLE POWDERS OF THE I90 COMPOSITIONS 35

FIGURE 21: WEIGHT LOSS AFTER CALCINATION, THE LOSS OCCURRING DUE TO THE EVAPORATION OF OXYGEN IS ALREADY SUBTRACTED (SEE EQUATION (17)) 36

FIGURE 22: AVERAGE WEIGHT LOSS (OUT OF 6 DISCS) OF SINTERED I90 SAMPLES WITH DIFFERENT ATMOSPHERE POWDERS (PZT…LEAD ZIRCONATE-TITANATE, PZ…LEAD ZIRCONATE, NC…NON CALCINED LEAD ZIRCONATE) 37

FIGURE 23: DENSITY GRADIENT OF I90 SAMPLES WITH RESPECT TO THE SINTER DESIGN USED, THE BLUE LINE INDICATES A SINTER DESIGN WHERE A SLIT WAS HELD OPEN UNDERNEATH THE CRUCIBLES WHEREAS THE SLIT WAS CLOSED DURING THE FINAL SINTER DESIGN (RED LINE) 38

FIGURE 24: XRD-SPECTRA OF I90 COMPOSITION AFTER CALCINATION, ONE CAN CLEARLY SEE THE PEROVSKITE MAIN PEAK AT ~30° 39

FIGURE 25: XRD SPECTRA OF I90 AFTER THE SINTERING STEP, MORE NARROW PEAKS CAN BE OBSERVED 39

Figure 26: XRD spectra of the M85 composition after calcination with the perovskite main peak at ~30° 40
Figure 27: XRD spectra of M85 compositions after sintering 40
Figure 28: Comparison of the volume of the unit cell and the composition of the sintered samples 41
Figure 29: Relative densities of the samples after sintering 42
Figure 30: Shrinkage in height and diameter, where the blue bars are indicating the shrinkage in diameter and the violet bars indicating the shrinkage in height 43
Figure 31: micrograph of non-doped I90 44
Figure 32: micrograph of non-doped M85 44
Figure 33: micrograph of full doped I90 44
Figure 34: micrograph of full doped M85 44
Figure 35: Comparison of grain sizes – yielded via the Line-Section-Method 45
Figure 36: Piezoelectric constant of the samples based on the I90 mixture 46
Figure 37: Piezoelectric constant of the samples based on the M85 mixture 46
Figure 38: Relative permittivity (ε) of the samples based on the I90 mixture prior and after poling 48
Figure 39: Loss factor (tanΔ) of the samples based on the I90 mixture prior and after poling 49
Figure 40: Hysteresis loops of single doped I90 compositions 49
Figure 41: Hysteresis loops of multi doped I90 compositions 49
Figure 42: Field/Current-loops of single doped I90 compositions 50
Figure 43: Field/Current-loops of multi doped I90 compositions 50
Figure 44: Strain-loops of single doped I90 compositions 50
Figure 45: Strain-loops of multi doped I90 compositions 50
Figure 46: Relative permittivity (ε) of the samples based on the M85 mixture prior and after poling 51
Figure 47: Loss factor (tanΔ) of the samples based on the M85 mixture prior and after poling 52
Figure 48: Hysteresis loops for single doped M85 compositions 53
Figure 49: Hysteresis loops for multi doped M85 compositions 53
Figure 50: Field/Current-loops for the single doped M85 compositions 53
Figure 51: Field/Current-loops for the multi doped M85 compositions 53
Figure 52: Strain loops for the single doped M85 compositions 53
Figure 53: Strain loops for the multi doped M85 compositions 53
Figure 54: High signal energy loss 54
Figure 55: 3D-Diagram of switching field vs. Goldschmidt's tolerance factor vs. effective mass at A-site for the M85 composition 55
Figure 56: micrograph of I90_Ba 61
Figure 57: micrograph of M85_Ba 61
Figure 58: micrograph of I90_Sr 61
Figure 59: micrograph of M85_Sr 61
Figure 60: micrograph of I90_BaSr 61
Figure 61: micrograph of M85_BaSr 61
Figure 62: micrograph of I90_Ca 62

FIGURE 63: MICROGRAPH OF M85_CA 62
FIGURE 64: MICROGRAPH OF I90_BACA 62
FIGURE 65: MICROGRAPH OF M85_BACA 62
FIGURE 66: MICROGRAPH OF I90_CASR 62
FIGURE 67: MICROGRAPH OF M85_CASR 62
FIGURE 68: IMAGE OF THE PHASE DISTRIBUTION IN A I90 SAMPLE, ON CAN SEE THE MATRIX (1), DARKER SECONDARY LEAD RICH PHASES (2) AND PORES 63
FIGURE 69: IMAGE OF A M85 SAMPLE SHOWING THE PHASE DISTRIBUTION, AGAIN A SECONDARY PHASE (2) WITH A HIGHER LEAD CONCENTRATION THAN THE MATRIX (1) CAN BE SEEN 63
FIGURE 70: I90_BACASR SAMPLE SHOWING A SECONDARY LEAD RICH PHASE (2), (1) INDICATES THE MATRIX 63
FIGURE 71: IMAGE OF THE M85_BACASR SAMPLE, AGAIN A LEAD RICH PHASE (2) CAN BE DETECTED 63

9 List of Tables

TABLE 1: SOME ALIOVALENT SUBSTITUENTS EITHER FOR A- OR B-SITE 13
TABLE 2: OVERVIEW OF FORMING TECHNIQUES [15] 17
TABLE 3: SAMPLE MATRIX, STOICHIOMETRIC QUANTITIES IN %MOL 26
TABLE 4: SINTER TEMPERATURES FOR SELECTED I90 COMPOSITIONS 34
TABLE 5: CALCULATED VALUES FROM XRD ANALYSIS 59
TABLE 6: DENSITY VALUES 60
TABLE 7: CHARACTERISTICS OF M85 COMPOSITIONS 64